

Nhan Nguyen

# **THE STATISTICAL ANALYSIS OF NOISE IN TRIAxIAL SENSOR**

Application in calibrating magnetometer

## ABSTRACT

Nhan Nguyen: The Statistical Analysis of Noise in Triaxial Sensor  
BACHELOR OF SCIENCE THESIS  
Tampere University  
Science and Engineering  
June 2019

---

This thesis demonstrates the statistical behaviour of noise in triaxial sensors, particularly magnetometers. The simple algorithm is proposed to support statistical tests. It is shown by statistical test that the sensor noise does not follow a Normal distribution as is commonly assumed. Beside noise, other sources of error corruption in magnetic field recording sensors are discussed. The combined effects of errors are demonstrated by a mathematical model containing translation, rotation and scaling factors. With this model, magnetometer readings are calibrated under the Maximum Likelihood Estimator scheme. The Least Square framework provides the unconstrained optimization problem with closed form solution. This solution can be used as initial guess for log-likelihood function. It guarantees that the algorithm converges to an accurate solution and reduces the number of iterations. Calibrated data is aligned to the sensor frame in order to be applied later in navigation applications, where the North finding problem is solved by true geomagnetic readings.

Keywords: Statistics, Inertial Navigation, Sensor Noise, Calibration, Magnetometer, Maximum likelihood estimator

The originality of this thesis has been checked using the Turnitin OriginalityCheck service.

## PREFACE

Firstly, I thank most to my supervisor, Dr. Philipp Müller, who has helped me a lot in objective thinking and gradually guided me to the research field with ambition and patience. Under his supervision, I had chance to discuss my ideas openly and be allowed to work independently. A lot of parts in this thesis are done with his help to find the right person, suitable keywords and meticulous guidance for a long period of time.

Besides, I showed my full gratitude towards Adj. Prof. Jussi Collin who supervised me for more than a year. This is the time when I knew more how to research, gain the working style and other technical knowledge that simplify my thesis path, my study and career tremendously.

I also appreciate Prof. Robert Piché for his fruitful idea in statistical distribution and optimization. Dr. Pavel Davidson with whom I built the foundation of magnetometer error knowledge, I do appreciate you.

I thank my friends Nga, Song, An and Tuan. You guys made my thesis days much shorter! It was a lot of fun having you nearby to chat and ease my daily stress. Finally, I express my gratitude towards my family in Vietnam. My relatives and especially my parents, for constantly supporting me during my study and also this thesis period.

Tampere, 1st June 2019

Nhan Nguyen

# CONTENTS

List of Figures . . . . .	iv
List of Tables . . . . .	v
List of Symbols and Abbreviations . . . . .	vi
1 Introduction . . . . .	1
2 Theoretical background . . . . .	4
2.1 Statistics and Probability . . . . .	4
2.1.1 Probability . . . . .	4
2.1.2 Statistics . . . . .	5
2.2 Magnetism . . . . .	6
2.2.1 History . . . . .	6
2.2.2 Earth's Magnetic Field . . . . .	6
2.2.3 Ferromagnetic materials . . . . .	8
2.3 Noise and its characterization . . . . .	9
3 Calibration method and Noise examination . . . . .	11
3.1 Magnetometer Errors Characterization . . . . .	11
3.1.1 Instrumentation Error . . . . .	11
3.1.2 Magnetic Deviation . . . . .	12
3.2 Complete error model . . . . .	13
3.3 Noise examination . . . . .	13
3.3.1 Noise Models . . . . .	13
3.3.2 Noise examination measurement plan . . . . .	14
3.3.3 Visualize the histogram . . . . .	15
3.3.4 Data anomaly and solution . . . . .	17
3.3.5 Fit probability distributions . . . . .	19
3.3.6 Goodness of fit . . . . .	19
3.4 Magnetometer Calibration method . . . . .	22
3.5 Alignment algorithm . . . . .	25
4 Result and Analysis . . . . .	26
4.1 Simulation results . . . . .	26
4.2 Experimental results . . . . .	28
5 Conclusion and Future Work . . . . .	30
References . . . . .	32
Appendix A Frame of Reference . . . . .	35

## LIST OF FIGURES

1.1	Figure-8 pattern [9] . . . . .	2
2.1	Probability density function of Normal distributions . . . . .	5
2.2	A permanent magnet and its created field lines. Image from [36] . . . . .	7
2.3	Sketch of the geomagnetic field. Image from [36] . . . . .	7
2.4	Earth's magnetic field with respect to Earth's geography [7] . . . . .	8
2.5	Magnetic domains and its modification in applied magnetic field [36] . . . . .	9
3.1	Non-orthogonal sensor's axes, x-axes of the sensor frame and Sensor are aligned . . . . .	12
3.2	Noise examination setup . . . . .	15
3.3	Androsensor application interface . . . . .	16
3.4	Histograms of applied rules to find bin width, y-axis reading, 2nd orientation	16
3.5	Bar graph of number of observations, y-axis reading, 2nd orientation . . . . .	18
3.6	Count histogram of applied Algorithm 1, y-axis reading, 2nd orientation . . . . .	19
3.7	Probability plot of data compared with CPDs . . . . .	20
3.8	Quantile-quantile plot of data compared with CPDs . . . . .	20
4.1	Simulation data of True and distorted magnetic field . . . . .	27
4.2	Simulation data of Calibrated magnetic field in Calibration and Optimized Sensor Frame . . . . .	27
4.3	Histogram of Euclidean distance between aligned-calibrated and true magnetic field . . . . .	28
4.4	Raw data with the sphere manifold reference . . . . .	29
4.5	Norm of calibrated data compared to raw data . . . . .	29
5.1	raw data of Figure-8 pattern in 3D space . . . . .	31
A.1	The relationship between different common used reference frames . . . . .	36
A.2	Sensor frame of reference . . . . .	36

## LIST OF TABLES

2.1	Different age groups of collecting data . . . . .	6
3.1	Number of bins calculated by statistical rules . . . . .	16
3.2	Parameter sets of used CPDs . . . . .	19
3.3	Best and second best probability distribution that noise follows on each axis, orientation from 2 statistical tests . . . . .	23
4.1	Calibration results . . . . .	27

## LIST OF SYMBOLS AND ABBREVIATIONS

$A$	Matrix $A$
$a$	Vector $a$
$ A $	determinant of matrix $A$
$A^{-1}$	Inverse of matrix $A$
$A^T$	Transpose of matrix $A$
CDF	Cumulative distribution function
CPD	Continuous Probability Distribution
$D(n)$	Set of $n \times n$ diagonal matrices
dim	Dimension of the object
DOF	Degree of freedom
$\mathbb{E}$	Expectation value of function
GEV	Generalized Extreme Value distribution
i.i.d	Independent and identically distributed random variables
LLF	Local-Level Frame
Matlab	a multi-paradigm numerical computing environment and proprietary programming language developed by MathWorks
MLE	Maximum Likelihood Estimator
$O(n)$	Set of $n \times n$ orthogonal matrices
PDF	Probability density function
$\mathbb{R}$	real numbers system
SVD	Singular Value Decomposition
tLS	t Location-Scale distribution

# 1 INTRODUCTION

From the ancient time, navigation had been the daily activity of primitive men. After foraging a whole day, they used natural landmarks such as mountains and trees to find the way back to their habitats. Over the time, humans utilized other celestial bodies to support their exploration. At noon, current position's altitude is determined by knowing altitude of the Sun, cooperated with the aid table providing declination of the Sun for the day. At night, the alternative is Polaris, the northern pole star. Using sextant in nautical navigation is an example of applying that method.

Gradually, vision showed their own drawbacks navigating on a cloudy day or unfamiliar place that people knew nothing about. In the 18<sup>th</sup> century, the Longitude determination was a famous problem which could not be solved by vision only. Instead, John Harrison created the Marine chronometer that utilized the periodic property of Earth's rotation to determine the longitude [30]. This method was an example that utilizes the characteristics of the Earth is the only solution instead of based on any human senses.

Exploiting natural elements of the Earth in navigation was not a breakthrough idea of the 18<sup>th</sup> century. The magnetic field of the Earth has been utilized for several centuries in estimating the North-South direction by navigators. Indeed, Chinese people designed one of the oldest magnetic compasses 10 centuries ago [19]. Nowadays, the contemporary technology in magnetometers such as optical magnetometry or superconducting quantum interference devices are used in great-sized ships and research laboratories. The modern magnetometers, however, are not limited to high-grade market only. With the advancements in Integrated Circuit, magnetometers are miniaturized and can be used in portable devices. Those allowed pedestrian navigation to blossom, increasing the interest in mobile navigation usage.

These low-cost magnetometers, however, contain several sources of errors and induced noise from manufacturing limitation and magnetic distortion in the vicinity of the sensors. A calibration procedure is needed before any usage in finding heading angle or navigation could be implemented. Apps that utilize a compass, e.g. Google Maps, frequently ask users to make a figure-8 pattern to calibrate the compass readings (Fig. 1.1). The mechanism behind this calibration technique will be discussed in following chapters. Magnetic field readings are also corrupted by noise. The interpretation of noise, particularly in sensor from the mathematical point of view is investigated thoroughly. Finally, a simplified model of noise is shown such that one can apply an optimization method to calibrate magnetometer readings.

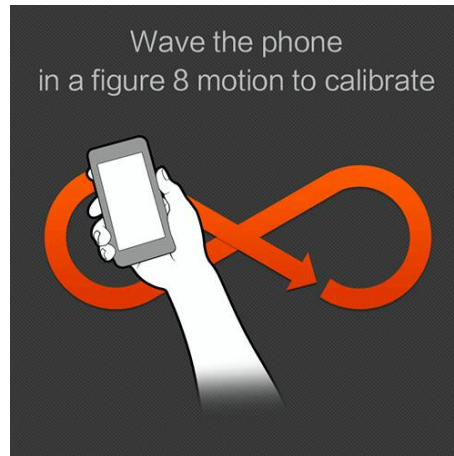


**Figure 1.1.** Figure-8 pattern [9]

Multiple approaches have been introduced to calibrate the magnetometers. The initial proposal was to put the magnetic sensor through a swinging process [2]. This technique requires to put the sensor set in several known orientations and compare those measurements with a noted reference. The disadvantages of this technique have been discussed in [11] and [25], reasoning the accuracy of aligning the set to known orientations.

The second method set, namely "attitude-dependent", is created to calibrate the magnetometers using the external heading information [23]. The need for external heading information all the time is the main limitation of this method.

The final set, which contains "attitude-independent" methods, is robust since it calibrates magnetometers without heading information. This class of method tries to fit the measurements to elliptical manifold. The batch least squares calibration algorithm derived in [8] and [11] solves the non-orthogonality, scaling and bias errors of magnetometers. The authors mentioned the inconsistency of estimated error parameters for calibration process in [8] and [25]. This inconsistency is discussed briefly in the thesis, while the thorough consideration can be found from [25], where the Adaptive Least Squares algorithm is proposed to tackle this problem.

Among recent articles, [33] is one of the first papers tackling the statistical property of noise in sensor. The derived calibration algorithm under Maximum Likelihood Estimator [MLE] framework which estimates the error parameters is shown to be robust from the statistical point of view. Inspired by the method, this thesis reviews the calibration procedure and provides further derivations within the MLE framework.

To the best of the author's knowledge, no state-of-the-art work in this field mentions the non-Normal distribution of sensor noise. This is mostly due to the burden of investigating the probability distribution that sensor noise follows best, and the simplicity of the likelihood function when assuming Gaussian distribution with similar standard deviation for all axes.

In this work, the best probability distribution that readings of each axis of the magne-

tometer follow is examined. The challenges in using statistical tests to choose the best distribution are also discussed. The thesis also proposes an algorithm that does not assume any sources of error from data anomaly or distorts the measurements, however, can still partially solve the statistical test challenge.

The complete magnetometer error model and how to calibrate the readings according to this model is shown. This thesis also mentions the alignment of calibrated readings such that the calibrated data could be used to find orientation. Finally, the simulation and experimental work are shown to demonstrate the success in calibrating a magnetometer.

This paper is organized as follows. Chapter 2 introduces the knowledge of statistics and probability. It also shows the property of the Earth's magnetic field, the error caused by magnetic sources and noise distortion in electrical devices. Chapter 3 characterizes each type of tri-axial sensor error, the combined error effect in one model and sensor noise examination procedure. Then, the simulation and experimental results of calibration, alignment algorithms are shown and analyzed in chapter 4. Finally, chapter 5 summarizes this thesis and comments on future work.

## 2 THEORETICAL BACKGROUND

In this chapter, we first give an overview of Statistics and Probability theory. Furthermore, we show the obstacle when moving from theoretical probability to numerical data presentation in statistical point of view (Section 2.1). Next, the magnetic field, particularly the field of the Earth, is represented. We also demonstrate how to find Geographic North with the knowledge of geomagnetic field and how magnetic material could affect readings of magnetometer in Section 2.2. Finally, noise characterization is discussed to link probability with sensor noise in Section 2.3.

### 2.1 Statistics and Probability

#### 2.1.1 Probability

Probability is "the extent to which an event is likely to occur, measured by the ratio of the favourable cases to the whole number of cases possible" [1]. The classic example comes from tossing a fair coin. The probability of getting head or tail each equals 0.5. It means one has 50% of observing head, similarly, tail when tossing that coin. The condition is that the sum of all independent events is 1 (100%).

Tossing a coin is an example of discrete random variable where a probability of an event is assigned a value. However, describing probability of a continuous random variable commonly requires a probability density function (PDF). This function describes the probability that value of an event belongs to an interval by computing the area under the PDF curve of that interval. One of the most popular continuous probability distributions (CPD) is the Normal or Gaussian distribution, which is described by the PDF

$$p(x|\mu, \sigma) = \frac{1}{\sqrt{2\pi\sigma^2}} e^{-\frac{(x-\mu)^2}{2\sigma^2}} \quad (2.1)$$

where  $x$  is the random variable,  $\mu$  is the mean and  $\sigma$  is the standard deviation of the distribution. As shown in Figure 2.1, the PDF of the Normal distribution has 2 parameters. Modifying these parameters shifts and changes the shape of the PDF graph (2.1) respectively. The next section demonstrates how to express probability of an event from experimental data.

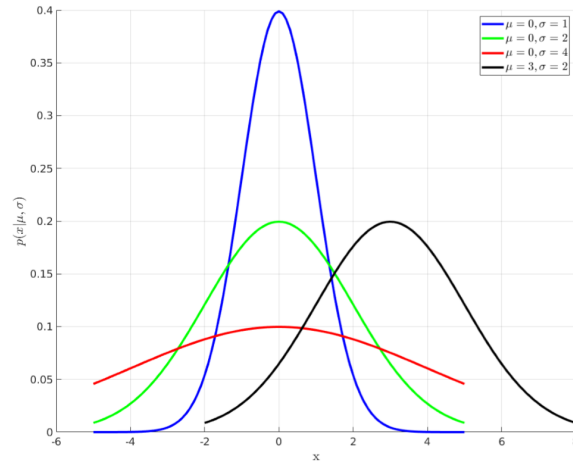


**Figure 2.1.** Probability density function of Normal distributions

## 2.1.2 Statistics

Statistics is "the practice or science of collecting and analyzing numerical data in large quantities, especially for the purpose of inferring proportions in a whole from those in a representative sample" [1]. A histogram is used to examine the distribution of discrete or continuous random variables.

When collecting numerical data, from any devices, we only receive finite different values in an interval. This is mostly due to the finite number of bits represented in any machine or the error (significant number) in the device that does not allow it to have more decimals than a threshold value. It is, thus, yielding a significant problem to describe PDF of continuous random variable by histogram of data. Statisticians and mathematicians overcame the difficulty by grouping data into so-called bins.

Let's assume ages of students in an arbitrary University are collected. The ages of first 50 students in the list are

$$\begin{bmatrix} 19 & 24 & 22 & 26 & 19 & 26 & 22 & 19 & 26 & 18 \\ 25 & 20 & 18 & 23 & 27 & 18 & 27 & 26 & 24 & 20 \\ 21 & 24 & 20 & 27 & 18 & 21 & 19 & 23 & 21 & 19 \\ 23 & 24 & 27 & 18 & 25 & 20 & 20 & 23 & 23 & 19 \\ 19 & 25 & 19 & 22 & 26 & 26 & 19 & 19 & 22 & 20 \end{bmatrix}$$

There are numerous ways to define the group, 3 of those are shown in table 2.1. No best ways of choosing bin width have been found since each bin sizes explores particular properties of the data. Grouping data into bins was done in 17<sup>th</sup> century by work of Graunt. However, no systematic guidelines were provided until Sturges' work in 1926 [27]. There are couple of established rules (including Sturges' rule) that provide the suitable width of bins and how to group data. A rule that is more appropriate for the features of the data represents the shape of distribution better. Besides, bin width is

**Table 2.1.** Different age groups of collecting data

Age group 1	Frequency	Age group 2	Frequency	Age group 3	Frequency
18-23	33	18-20	21	18-19	15
24-25	7	21-26	25	20-25	25
26-27	10	> 26	4	26-27	10
<b>Sum</b>	50		50		50

an undeniably vital factor to assess how good data follows a distribution, which will be studied rigorously in following sections.

## 2.2 Magnetism

### 2.2.1 History

Magnetic phenomena have been observed since 600 BC by Greek philosophers. They described the magnetic properties of natural ferric ferrite ( $Fe_3O_4$ ) stones (lodestones) [15]. In 1269 came the first detail description of a compass, made by Petrus Peregrinus de Maricourt. The French scholar used iron needles to visualize the magnetic field on the surface of a spherical magnet [17]. By his work and others, magnetic field was step-by-step granted the properties of a vector field - a vector quantity that is connected with each point in space [36]. The properties were later utilized in multiple applications, ranging from Mass Spectrometry, Cathode Ray Tubes in non-flat-screen TVs to Magnetic Resonance Imaging (MRI). In pedestrian navigation, magnetic fields are valuable in estimating North-South direction.

### 2.2.2 Earth's Magnetic Field

A magnetic field is denoted by the symbol **B**. The direction of **B** at a location is direction that north-pole of a compass needle points to. The magnetic field is visualized by magnetic field lines whose direction at a point is tangent to the magnetic field vector **B** at that point (Fig. 2.2).

The geomagnetic field is the magnetic field of the Earth that exists from inside the Earth's core to the outer space. This field is generated by a molten iron stream in the outer core of the Earth. This generated process is called geodynamo which describes the heat withdraw from the Earth's core [35]. The geomagnetic field, thus, in the simplest model could be demonstrated by the bar magnet (Fig. 2.3).

The geomagnetic field preserves the following characteristics

- Intensity: The field ranges from approximately 25 microtesla ( $\mu T$ ) in the vicinity of

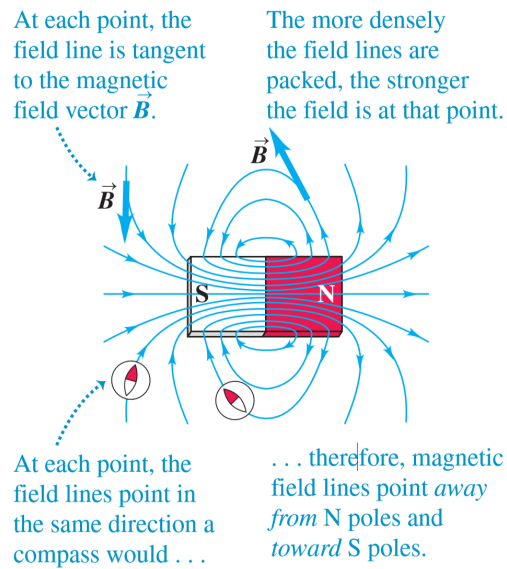


**Figure 2.2.** A permanent magnet and its created field lines. Image from [36]

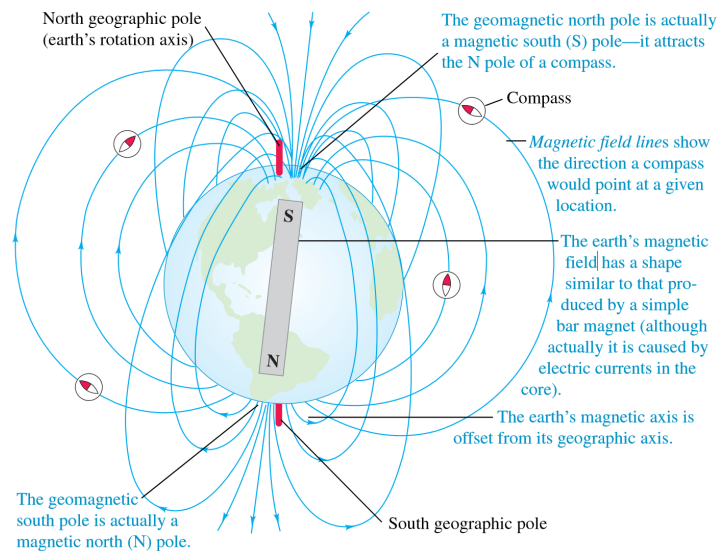


**Figure 2.3.** Sketch of the geomagnetic field. Image from [36]

the equator to around  $75 \mu T$  near the poles [31].

- Declination: The deviated angle between magnetic North and the geographic North.
- Inclination: The angle between the magnetic field and the plane tangential with local position. (Fig. 2.4).
- Variation: The causes of alternation are from ionosphere's currents and Earth's interior disturbances. Those produce daily fluctuations of magnetic field of around 25 nanotesla ( $nT$ ), while rarely, the superimposed oscillations of about  $1 nT$  happens in a period of few seconds [31].

The inclination and declination angles provide the information for heading and orientation determination. After measuring the magnetic field at the current location and obtaining the geomagnetic field vector, one can deduce the heading angle of a device with respect

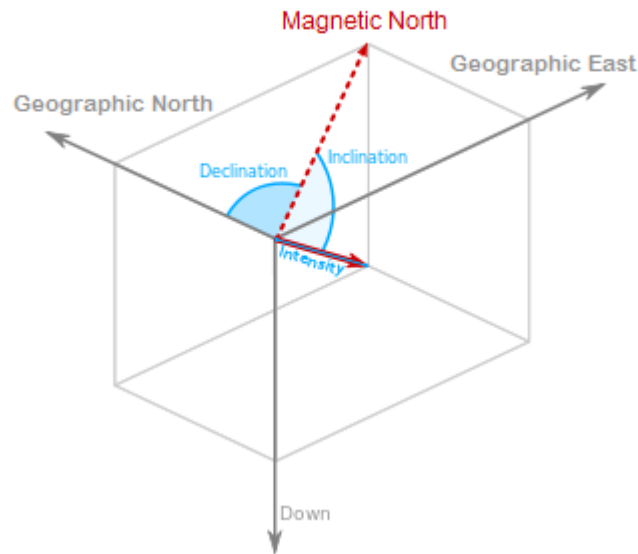


**Figure 2.4.** Earth's magnetic field with respect to Earth's geography [7]

to the magnetic North. Let  $h_x$ ,  $h_y$  and  $D$  be  $x$ ,  $y$  components of the geomagnetic field and the local declination respectively. Then, the geographical azimuth  $\phi$  is

$$\phi = \tan^{-1} \left( \frac{h_y}{h_x} \right) + D \quad (2.2)$$

Calibrating a magnetic field measurement is an essential step in heading determination by obtaining correct values of  $h_x$ ,  $h_y$  in (2.2). The declination angle at the current location is available from geomagnetic charts and software [20].

The small variation of the geomagnetic field simplifies the calibration procedure. Indeed, the small change in amplitude of the geomagnetic field in the calibration procedure (less than 5 mins) is smaller than the resolution of most MEMS based magnetometers. Thus, the Earth's magnetic field can be considered constant over time.

### 2.2.3 Ferromagnetic materials

There are 3 types of magnetic materials: paramagnetic, diamagnetic and ferromagnetic substances [36]. The first two types are out of scope for magnetometer calibration. The final type is ferromagnetic materials, including iron, nickel, cobalt, etc is of interest. In ferromagnetic materials, strong interactions between atomic magnetic moments make them aligned to each other in the region called magnetic domains. Figure 2.5 shows an example of magnetic domain structure. Within each domain, nearly all of the atomic magnetic moments are parallel. The domain magnetizations are randomly oriented when there is no applied field. However, when there exist an external field, it orients those domains and makes them aligned with itself. This magnetizes the material. Besides, it causes shift in the boundaries of magnetic domains. While domains which are magnetized in the field

direction grow, those in different direction shrink. The condition when domains could not grow anymore is called saturation magnetization. At that time, increasing the external field does not increase magnetization of the material.

In some cases, a material is magnetized by an external magnetic field reserves magnetization despite the disappearance of external field. This behavior is characteristic of permanent magnets. In magnetometer calibration context, this is related to hard iron material. By contrast, soft iron materials that are ferromagnetic materials are easily magnetized and demagnetized with a small change of magnetic field. Thus, soft iron is used to produce electromagnets.

Beside distorted by error sources that have no random behaviors (e.g. hard iron), magnetometer readings are also affected by a stochastic phenomenon called noise. Sensor noise is discussed in the next section.

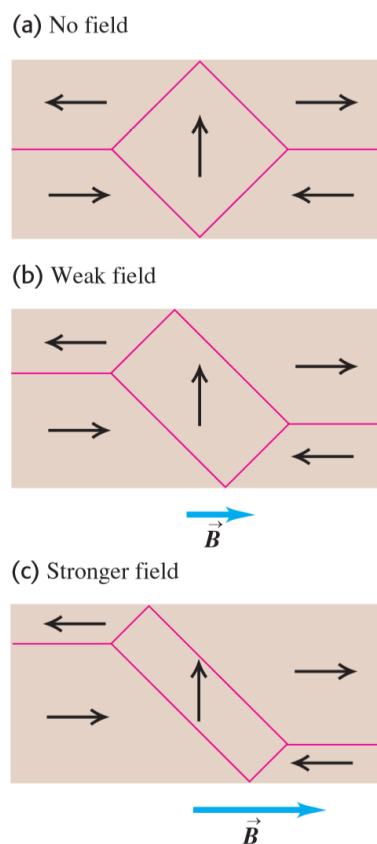


**Figure 2.5.** Magnetic domains and its modification in applied magnetic field [36]

## 2.3 Noise and its characterization

Noise, which is different from acoustic noise, is defined as "irregular fluctuations that accompany a transmitted electrical signal but are not part of it and tend to obscure it" [1]. In this thesis, the magnetometer AKM09918 from Asahi Kasei Microdevices corporation is the subject of calibration [16]. This sensor is a tri-axial electronic compass Integrated

Circuit that uses the Hall effect to measure the magnetic field. It requires meticulous research to examine the block diagram in the datasheet of sensor, address the collective interference of its components as well as its interaction with other elements of a smartphone. Generally, the whole system is exposed to intrinsic noise (the noise generated inside an investigated device) and extrinsic noise that is situated outside the investigated circuit [34]. These two noise types can be referred to electrical noise, static noise and noise from digital circuits. A typical example of electrical noise is thermal noise, it originates from the random motions of free electrons inside a piece of conductive material. Other types of noise which are due to processing, temperature variation, ageing, etc are discussed thoroughly in [34].

Intrinsic noise is essentially random in nature and requires a statistical description while extrinsic noise is usually of a deterministic nature [34]. Thus, extrinsic noise can be associated with the joint effect of other error types. By treating intrinsic noise in each axis as a random variable, CPD could be used to model it.

The next chapter formulates each type of errors in magnetometer measurements and demonstrates the procedure to study sensor noise on each axis.

## 3 CALIBRATION METHOD AND NOISE EXAMINATION

### 3.1 Magnetometer Errors Characterization

Inspired by error characterization work, especially from [25], [32], the modelled errors from low-cost magnetometer are divided into two categories. The first category represents the instrumentation errors including sensor offsets, scale factor and non-orthogonality of sensor axes. These errors are due to fabrication limitations. The second category is magnetic deviation. The magnetic deviation is caused by interference of sensor with ferromagnetic compounds in the vicinity of the host platform. Those are divided into permanent magnetism and induced one or hard iron and soft iron effect respectively. Other types of non-modelled error, which include generic and more complex effects related to sensor-specific characteristics and magnetic distortion, are not the scope of this thesis.

#### 3.1.1 Instrumentation Error

##### Sensor offset

Sensor offset or bias is the measurement reading of triaxial sensors in the magnetic-free field. It could be modelled as the constant vector  $\mathbf{b}_{SO} \in \mathbb{R}^3$  [33].

##### Scale factor

This error is originated from the sensitivity of the axis of sensor. Although being placed to measure the same magnetic field, 2 sensors could produce different readings.  $\mathbf{T}_{SF} \in D^+(3)$  is a mathematical formulation of this error, where  $D^+(n) = \{\mathbf{A} \in D(n) : \mathbf{A} > 0\}$ . [24].

##### Non-orthogonality

When the sensor axes are aligned properly, the field parallel to one axis is measured by that axis only. When the axis set is misaligned, however, that field is observed by other axes. Fig. 3.1 represents the 3 orthogonal sensor frame axes and misaligned sensor's axes. Let  $\epsilon_x, \epsilon_y, \epsilon_z$  be directions of x,y and z axes of sensor in the sensor frame. X-axis of sensor and sensor frame are aligned to see the misalignment of other 2 axes. The definition of frame and common use frames of reference are introduced in the Appendix A. The effect of non-orthogonality is represented by

$$\mathbf{T}_{NO} = [\epsilon_x, \epsilon_y, \epsilon_z]^{-1} \in \mathbb{R}^{3 \times 3}.$$

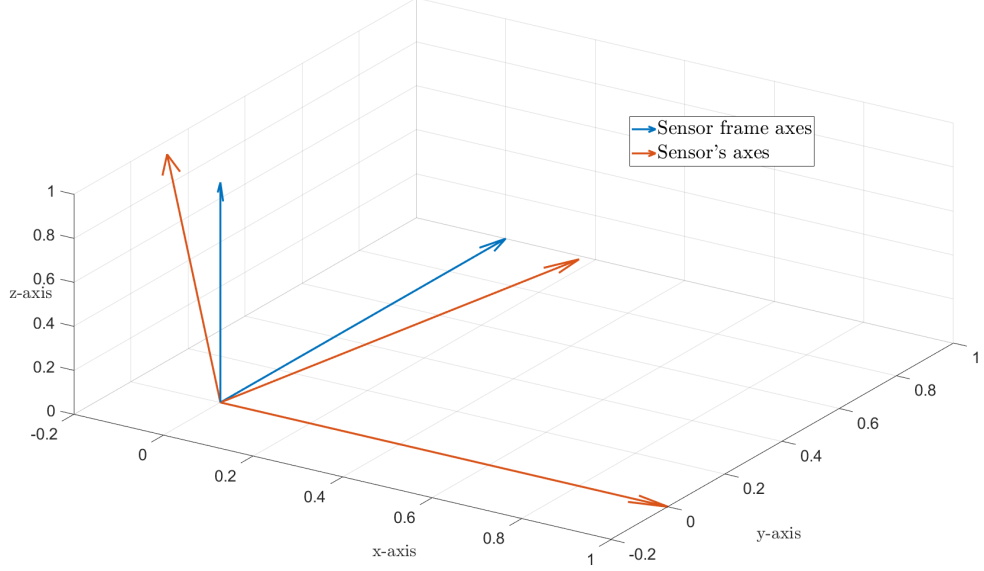


**Figure 3.1.** Non-orthogonal sensor's axes, x-axes of the sensor frame and Sensor are aligned

### 3.1.2 Magnetic Deviation

**Hard iron** As mentioned in section 2.2.3, hard iron is the effect caused by permanent magnets inherent to the sensor frame. These could be materials in the device carrying magnetometer or elements of magnetometer itself. Hard iron effect is a constant bias:  $\mathbf{b}_{HI} \in \mathbb{R}^3$ .

**Soft iron** The soft iron material is assumed to attach to the sensor frame of the magnetometer. The magnitude and the direction of the magnetic field induced by the soft iron effect depends on the incident angle of the Earth's magnetic field on that material. The induced magnetic field vector  $\mathbf{h}_{SI}$  can be presented as a transformation of the Earth's magnetic field, producing

$$\mathbf{h}_{SI} = \mathbf{T}_{SI} \mathbf{R}_{LLF}^S \mathbf{h}_{LLF} = \mathbf{T}_{SI} \mathbf{h}^S,$$

where  $\mathbf{T}_{SI} \in \mathbb{R}^{3 \times 3}$  is the soft iron transformation matrix,  $\mathbf{R}_{LLF}^S$  is the rotation matrix from LLF to the sensor frame,  $\mathbf{h}^{LLF}$  is the geomagnetic field in LLF. In this work, there is no further simplification on the nature of soft iron to ease the calibration procedure while some existing work models soft iron transformation as diagonal matrix. Detail explanation of Magnetic deviation can be found from [33]. The next section combines all aforementioned errors into a model.

## 3.2 Complete error model

Instrumentation error and magnetic deviation can be combined into a single model as follows [33]

$$\mathbf{h}_{r,i} = \mathbf{T}_{SF}\mathbf{T}_{NO}(\mathbf{T}_{SI}\mathbf{h}_i^S + \mathbf{b}_{HI}) + \mathbf{b}_{SO} + \epsilon_i \quad (3.1)$$

where  $\mathbf{h}_{r,i}$  is the trial magnetometer reading at  $i^{th}$  index,  $\mathbf{h}_i^S$  is the geomagnetic field in the sensor frame,  $\mathbf{T}_{SF}$ ,  $\mathbf{T}_{NO}$ ,  $\mathbf{T}_{SI}$ ,  $\mathbf{b}_{HI}$  and  $\mathbf{b}_{SO}$  are error sources described in previous sections.  $\epsilon_i \in \mathbb{R}^3$  is wideband noise from each axis of sensor.

Without loss of generality, the magnetometer reading can be described by

$$\mathbf{h}_{r,i} = \mathbf{T}\mathbf{h}_i^S + \mathbf{b} + \epsilon_i \quad (3.2)$$

where  $\mathbf{T} = \mathbf{T}_{SF}\mathbf{T}_{NO}\mathbf{T}_{SI}$  and  $\mathbf{b} = \mathbf{T}_{SF}\mathbf{T}_{NO}\mathbf{b}_{HI} + \mathbf{b}_{SO}$  denote total transformation and bias effect respectively. Since  $\mathbf{T} \in \mathbb{R}^{3 \times 3}$  and  $\mathbf{b} \in \mathbb{R}^3$  are unconstrained, unmodelled linear time-invariant magnetic errors and distortions are also taken into account.

Section 2.2.2 mentions that the geomagnetic field is constant in the calibration procedure, i.e.  $\mathbf{h}_i^{LLF}$  is constant. After another constant rotation, the obtained geomagnetic field in the sensor frame  $\mathbf{h}_i^S$  is also constant, i.e. rotating a constant vector  $\mathbf{h}_i^{LLF}$  around the origin yields the spherical surface which is made from  $\mathbf{h}_i^S$ . The magnetometer readings  $\mathbf{h}_{r,i}$  without noise, thus, lie on an ellipsoidal surface. The proof uses the property of Singular Value Decomposition (SVD) [24] where  $\mathbf{T} = \mathbf{U}\mathbf{\Sigma}\mathbf{V}^T$  is the SVD decomposition of matrix  $\mathbf{T}$ .  $\mathbf{V}$  and  $\mathbf{U}$  are orthogonal matrices that rotate the manifold, while  $\mathbf{\Sigma} \in D^+(3)$  scales 3 orthogonal axes of the sphere to make it an ellipsoid. The rigorous proof is presented in [33].

Define  $\mathbf{h}_i^C := \mathbf{V}^T\mathbf{h}_i^S$  as the geomagnetic field in the calibration frame  $\{C\}$ , which is obtained by the orthogonal transformation  $\mathbf{V}^T$  from the sensor frame  $\{S\}$ . The mathematical model (3.2) becomes

$$\mathbf{h}_{r,i} = \mathbf{U}\mathbf{\Sigma}\mathbf{h}_i^C + \mathbf{b} + \epsilon_i, \quad (3.3)$$

where  $\mathbf{U}$ ,  $\mathbf{\Sigma}$  and  $\mathbf{b}$  are estimated in calibration process. However, the rotation matrix  $\mathbf{V}$  will not be observed in this process if  $\mathbf{h}_i^S$  and  $\mathbf{h}_i^C$  are not measured. This issue will be discussed in the last section of this chapter. We are using the MLE framework to estimate  $\mathbf{U}$ ,  $\mathbf{\Sigma}$ ,  $\mathbf{b}$  which requires the probability distribution of noise. Thus, which type of CPDs the noise in each axis follows needs meticulous study.

## 3.3 Noise examination

### 3.3.1 Noise Models

In this section all continuous probability distributions available in Matlab R2019a [18] are examined, whether they describe the noise distribution on the three axes of triaxial sen-

sors sufficiently well. In order to be tested with actual sensor data, a chosen distribution had to fulfill two criteria.

- The CPD is accepted when it was not proposed for a specific problem. If the distribution was developed to model a specific phenomena, those should have relation to intrinsic noise of sensors. For example, Birnbaum-Saunders Distribution is rejected since it was used to model fatigue life of a metal subject to cyclic stress [5], which is not related to noise in magnetometer measurements.
- The CPD has zero mean or median since there is no reason that noise is more probable to yield positive or negative values. Besides, the offset term in equation (3.3) already compensates for the non-zero mean/median. Thus, the chosen CPD should have zero mean/median and both negative, positive support [13].

The first criterion reduces the number of suitable CPDs to ten. After the second criterion, the five candidates left for modeling noise are: Extreme Value, Generalized Extreme Value (GEV), Logistic, Normal and t Location-Scale (tLS) distributions. The measurement plan is introduced in order to check which aforementioned distributions the noises in each axis of the sensor follow.

### 3.3.2 Noise examination measurement plan

#### Device setup

The experimental tests have been conducted in the open area ( $61^{\circ}27'03''N, 23^{\circ}49'01''E$ ) on the bank of Särkijärvi lake in Tampere, Finland. The site's location was chosen to ensure a clean environment in terms of artificial magnetic field anomalies and free-magnetic field exposure except of the geomagnetic field. The vibration of location is assumed to have negligible effect on measurements.

The Android device is put stationary for 5 minutes. The tests were conducted in 6 different orientations of the sensor frame as shown in Fig. 3.2 to examine patterns of noise on each axis in 3 Degree of Freedoms (DOF). Each DOF contains measurements on both positive and negative axes. This measurement setup offers two studies:

- Similarity in true geomagnetic field and noise. For example, without noise the magnetic field readings in the sensor frame on x-axis of orientation 1 should equal readings on y-axis of orientation 2, z-axis of orientation 3 or negative values on y-axis of orientation 4, etc. Secondly, it is possible to study the pattern in noise of different axes measuring the same value such as x-axis of orientation 1 and y-axis of orientation 2.
- Diversity: One axis is used to measure the geomagnetic field in different orientations, e.g. x-axis of the sensor frame is used to measure the magnetic field in 3 DOFs as in orientations 1, 2 and 3.

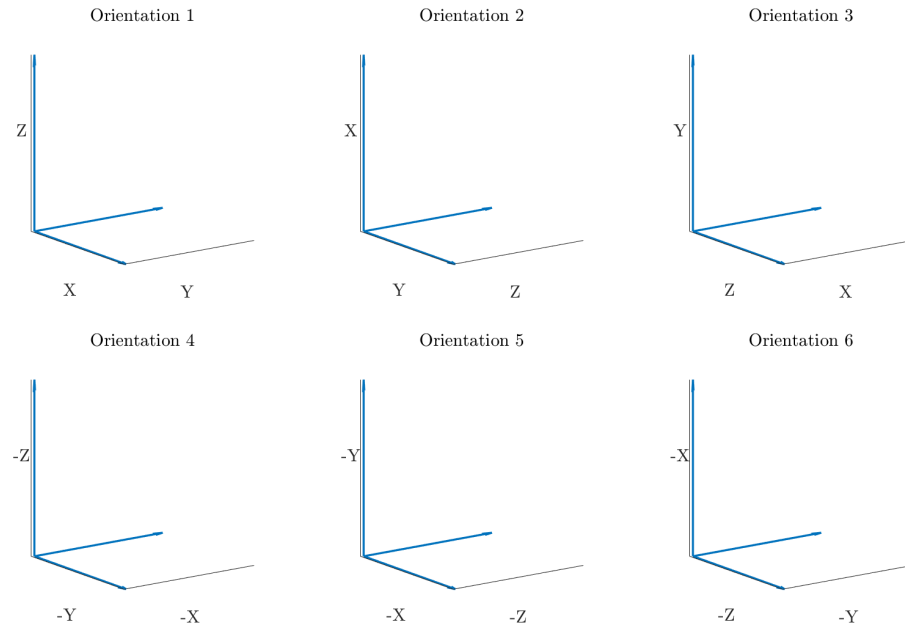


**Figure 3.2.** Noise examination setup

## Device info

The sensor used for noise examination was an AK09918 3-Axis Electronic Compass from Asahi Kasei Microdevices Corporation [16].

## Acquisition Unit

The sensor is embedded in a phone HUAWEI P Smart with Android operating system. The AndroSensor application [4] is used to log raw sensor data. It is sampled at 15ms period, the user interface of the app is shown in Fig. 3.3. Data is stored on the phone and analyzed later on a computer. The yellow box on the left is used to start logging data and the yellow box on the right to change the settings (value of period, units of measurement, logged sensors, etc).

### 3.3.3 Visualize the histogram

Since the sensor stays still in each orientation, measurement readings in one axis are the summation of a constant value and noise (Equation 3.3). Different rules are applied to find bin width and visualize histogram [12], [26], [29]. Magnetometer data of y-axis in the second orientation is used as example for noise examination. Fig 3.4 shows histograms of this data for different bin widths. The values of bin widths for different rules are shown in Table 3.1.

Each rule was proposed for a specific purpose, e.g. Sturge's rule is derived from binomial



Figure 3.3. Androsensor application interface

Table 3.1. Number of bins calculated by statistical rules

Sturge/Doane	Freedman-Diaconis	Scott	Rice	Shimazaki and Shinomoto
16	62	60	55	48

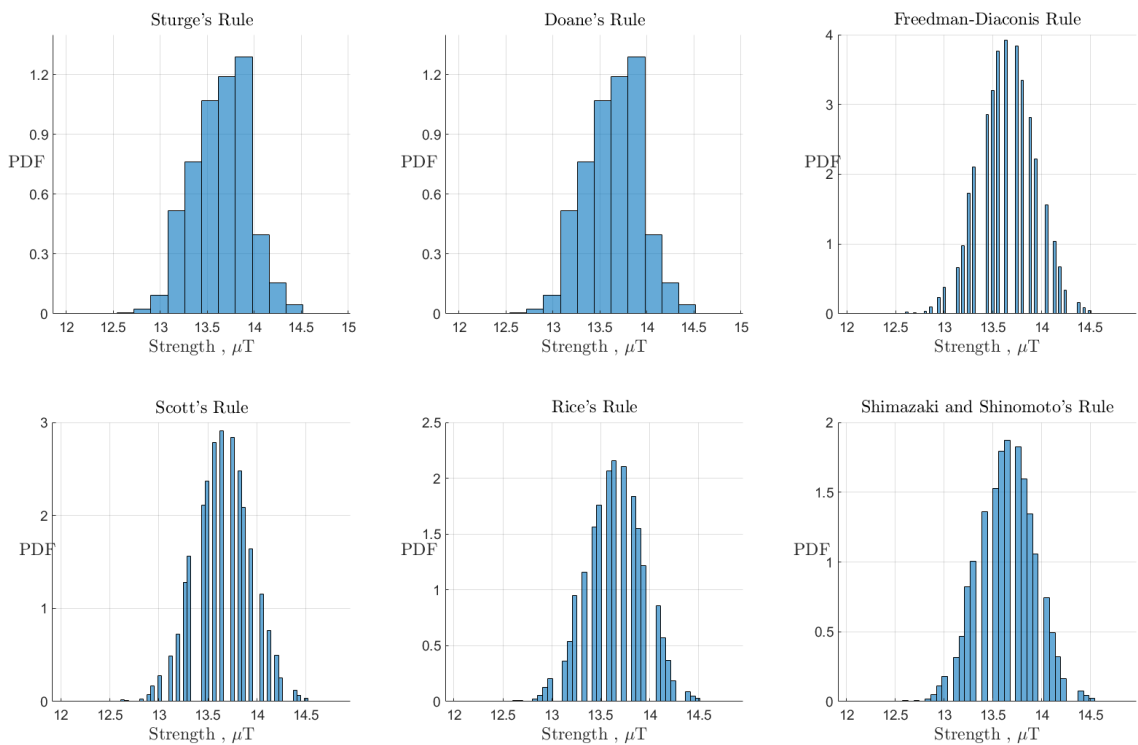


Figure 3.4. Histograms of applied rules to find bin width, y-axis reading, 2nd orientation

distribution and implicitly assumes an approximately Normal distribution, which may be not true in this case. None of those rules are designed for specific data type containing anomalies. As the result, we encounter the bins with no probability (empty bins) for each of last four rules in Fig 3.4. This yields a significant problem when comparing the goodness of fit of different CPDs by both  $\chi^2$  and Kolmogorov-Smirnov test. For instance, the data contains N samples. If the  $k^{th}$  bin in a count histogram is empty while the expected number of observations for a CPD is non-zero, the result of the  $\chi^2$ -test is

$$\chi^2 = \sum_{i=1}^n \frac{(O_i - E_i)^2}{E_i} > \frac{(O_k - E_k)^2}{E_k} = E_k \rightarrow \infty \text{ as } N \rightarrow \infty, \quad (3.4)$$

where  $O_i$  is the observed number of samples and  $E_i$  is the expected number of samples of  $i^{th}$  bin in the count histogram. The hypothesis of  $\chi^2$  test is rejected no matter how small the level of significance. For instance, we have 20000 observations of y-axis of  $2^{nd}$  orientation. By using Shimazaki and Shinomoto's rule to create a count histogram and testing how good data follows the Normal Distribution by  $\chi^2$ -test, we have 35 bins that satisfy the condition of the  $\chi^2$ -test, i.e. 32 degrees of freedom (Section 3.3.6 explains the  $\chi^2$ -test and significance level more thoroughly). With 0.005 significance level, the rejection criterion of Null hypothesis in the  $\chi^2$ -test with 32 degrees of freedom is  $\chi^2 > 56.328$ . Empirically, the expected number of samples (3.4) near the mean value is in the order of 1000,  $\chi^2$  value will be greater than 1000. This will immediately rejects the null-hypothesis that noise follows Normal Distribution. Similarly, other 4 CPDs (Sec 3.3.1) are also rejected using  $\chi^2$ -test with that significance level.

### 3.3.4 Data anomaly and solution

The documentation of the AndroSensor application shows that the accuracy of raw data from the magnetometer is  $0.0625 \mu T$ , which is the resolution of measurements. Since noise is a continuous random variable, its values range in an interval. Due to the resolution of the recorded data, the measurements are grouped to values with  $0.0625 \mu T$  discrepancy, i.e. there should be observations every  $0.0625 \mu T$ . Collecting the measurement described in Section 3.3.2, there are 1576 observations with value  $13.4375 \mu T$  (+0), 1771 of  $13.5000 \mu T$  (+0.0625), 2080 of  $13.5625 \mu T$  (+2 · 0.0625), 2170 of  $13.6250 \mu T$  (+3 · 0.0625) and so on. Although this period should remain, there is no observation with value  $13.6875 \mu T$  (+4 · 0.0625). This leave-one-out every 5-bin pattern is observed again in the next 5 bins that finally yields Figure 3.5 showing the number of observations for each discrete reading value. Similar behaviors is observed also in X and Z axes of second orientation as well as for all three axes of the other orientations. Using another app called Sensor Record [28] yields similar patterns.

More research should be carried to understand the reason of this pattern in data. Since there exists no information on how data is recorded in sensors nor how they group data into these values, attempts to interpolate the empty bins to make data continuous lack

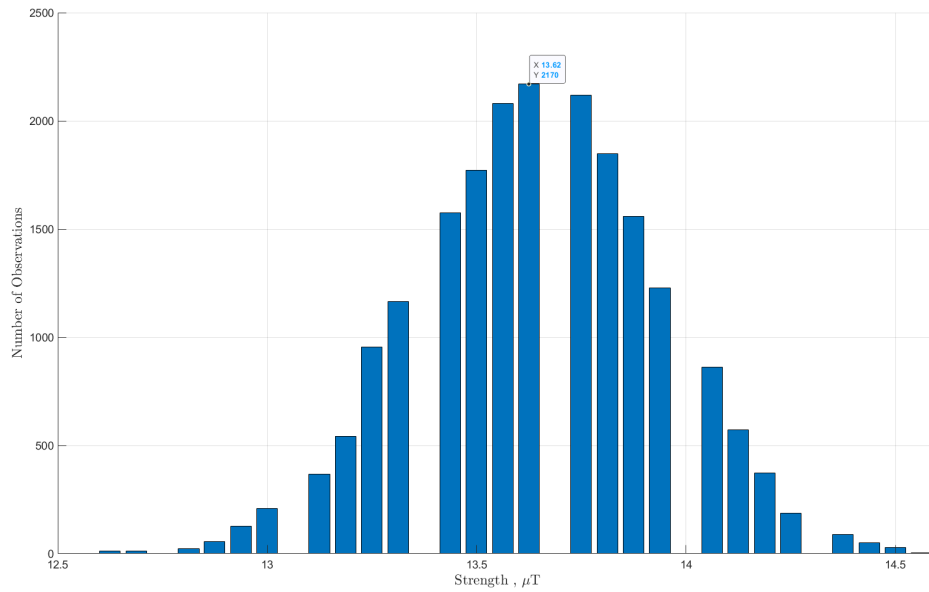


**Figure 3.5.** Bar graph of number of observations, y-axis reading, 2nd orientation

reasonable reference. Choosing appropriate bin widths, however, can solve the problem without the aforementioned effect (such as Sturge's Rule in Fig 3.4). To determine the number of bins, Algorithm 1 is proposed.

---

**Algorithm 1** Maximal approved number of bins

---

**Input:** Magnetometer measurements of t-axis  $h_r^t$

Resolution of AndroSensor:  $a = 0.0625 \mu T$

**Output:** The suitable number of bins  $n_{suit}$

1.  $M = \max(h_r^t); m = \min(h_r^t)$

2.  $n_M = \lceil \frac{M-m}{a} \rceil, n_m = \lfloor \frac{M-m}{2a} \rfloor$

3.

For  $n = n_M : -1 : n_m$

    If histogram of  $h_r^t$  with n bins contains no empty bins:

$n_{suit} = n;$

        break;

end

---

This algorithm guarantees to find the maximum number of bins such that the histogram contains no empty bins. The bin width is then simply  $\frac{M-m}{n_{suit}}$ . The greatest bin width that could be chosen is two times the resolution since it already assures no empty bin. The ceiling and floor functions are for already rounded measurements. Applying Algorithm 1 to the data described above yields the histogram in Fig 3.6.

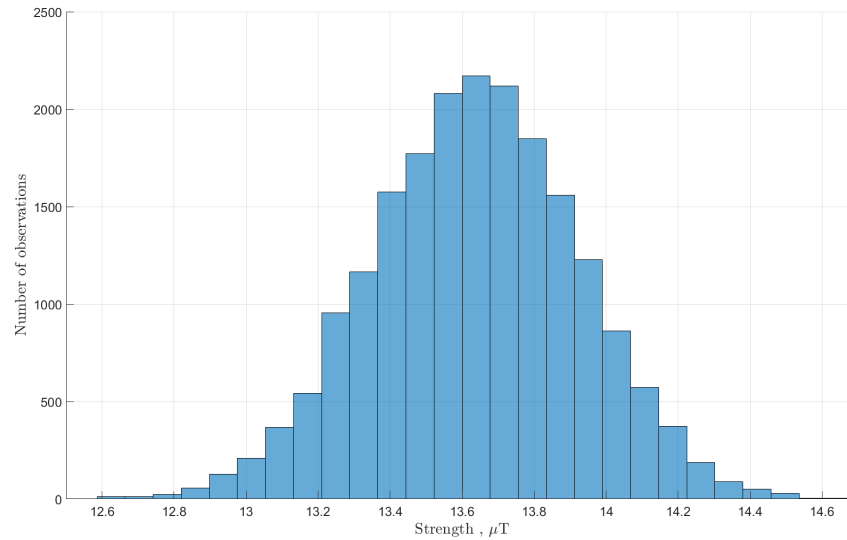


**Figure 3.6.** Count histogram of applied Algorithm 1, y-axis reading, 2nd orientation

**Table 3.2.** Parameter sets of used CPDs

Parameter	Extreme Value	GEV	Logistic	Normal	t Location-Scale
Location ( $\mu$ )	13.7903	13.5345	13.6475	13.6460	13.6463
Scale ( $\sigma$ )	0.2869	0.2912	0.1658	0.2903	0.2856
Shape		-0.2260			62.4351

### 3.3.5 Fit probability distributions

The PDFs of the five candidate CPDs are described by parameters, such as location, scale, shape parameters, etc. The built-in Matlab function "fitdist", which is based on the MLE method, is used to estimate those parameters. The estimated parameter sets of those five CPDs are shown in Table 3.2. The parameter set of each CPD is used to create the corresponding distribution by Matlab "makedist" function.

### 3.3.6 Goodness of fit

In order to evaluate which probability distribution fits best to the noise of the measurements, the two steps procedure is used.

#### Probability plot and Quantile-quantile plot

In the first step, the generated analytic probability distribution is compared with distribution of noise by visualization. Functions "probplot" and "qqplot" from Matlab are used. This method cannot evaluate which distribution is better. However, it can be used to re-

move unsuitable distributions since the measurement should fall on the reference line of analytical probability distribution, or at least approximately similar number of data points should fall on both sides of the line (Fig 3.7, 3.8).

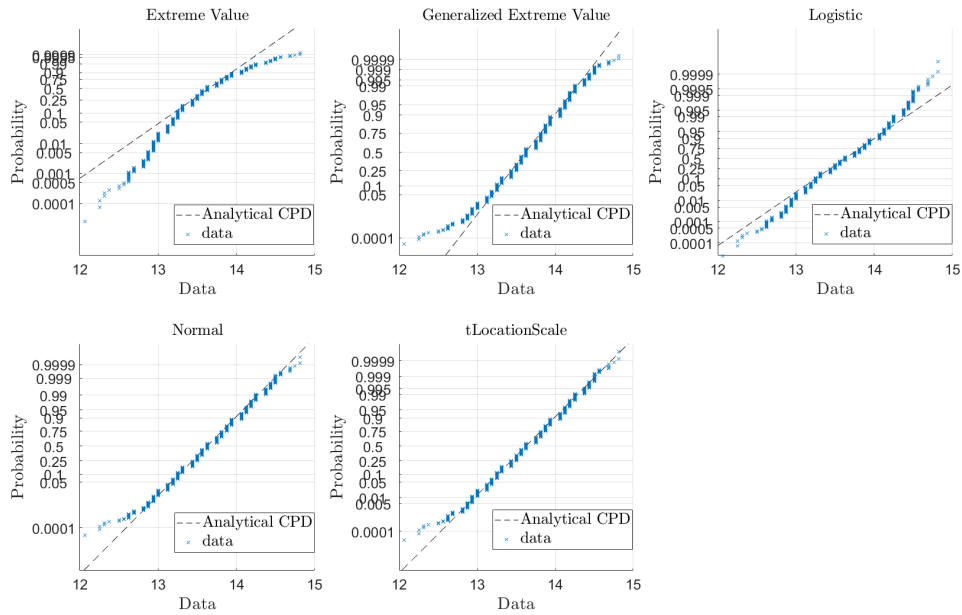


**Figure 3.7.** Probability plot of data compared with CPDs

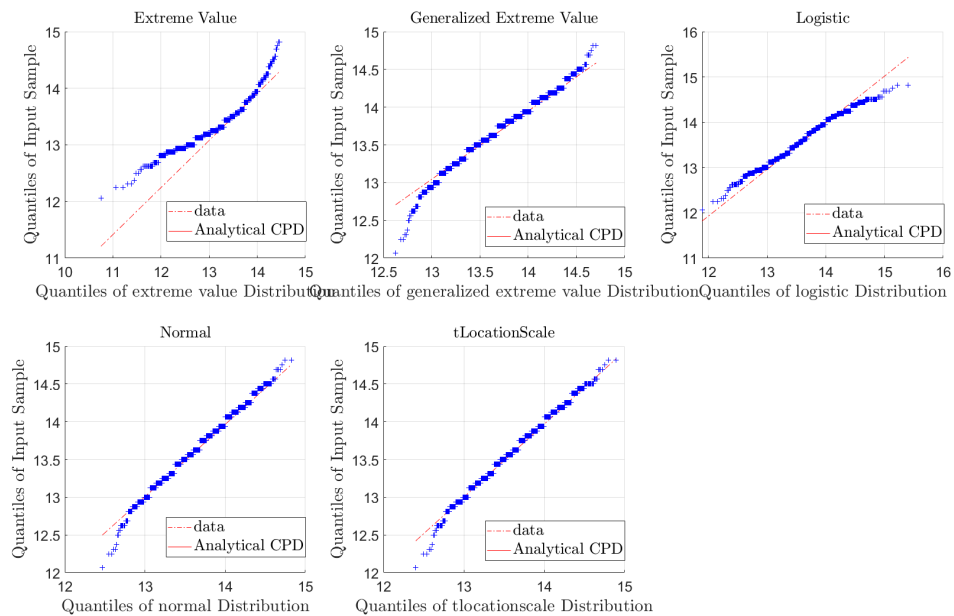


**Figure 3.8.** Quantile-quantile plot of data compared with CPDs

In both figures, samples fall out of the reference line of analytical Extreme Value distribution as well as distribute not evenly between both sides of that line. Because this pattern is observed from data of all other orientations, Extreme Value distribution is removed from the suitable distribution set.

## $\chi^2$ and Kolmogorov-Smirnov tests

In the second step, the best probability distribution function that noise on each axis follows is chosen by statistical tests. The statistical hypothesis testing applied in this case is: Assume our samples  $X$  follow the unknown probability distribution  $F_X(x)$ . With  $\alpha$  level of significance, we need to evaluate the hypothesis

- Null hypothesis  $H_0: F_X(x) = F^*(x)$
- Alternative hypothesis  $H_1: F_X(x) \neq F^*(x)$

where  $F^*(x)$  is the known probability distribution. Let  $F_X^n(x)$  be empirical PDF built from  $n$  samples, then

$$\lim_{n \rightarrow \infty} F_X^n(x) = F_X(x)$$

Since we never have infinite samples,  $F_X^n(x)$  is not exactly the same as  $F_X(x)$ . The level of significance  $\alpha$  can be used to state the level of confidence in the hypothesis test.

The Pearson's chi-squared test ( $\chi^2$ ), which can be found in many statistics book, for example [22], is defined as follows

$$g = \sum_{i=1}^n \frac{(O_i - E_i)^2}{E_i} \sim \chi^2(n - r - 1) \quad (3.5)$$

where  $n$  is the number of bins,  $O_i$  is the observed and  $E_i$  is the expected number of samples in the  $i^{\text{th}}$  bin. The degree of freedoms is  $(n - r - 1)$  where  $r$  is the number of parameters in PDF  $F^*(x)$ . For example, the Normal distribution has two parameters which are mean and standard deviation. Using the significance level  $\alpha$ , we define the variable  $\chi = H_{\chi^2(n-r-1)}^{-1}(1 - \alpha)$ , where  $H_{\chi^2(n-r-1)}$  is the cumulative distribution function of  $\chi^2$ . This means, if  $y \sim \chi^2(n - r - 1)$ , the probability that  $y \leq \chi$  is  $1 - \alpha$ . The Null hypothesis is rejected when  $g > \chi$ . Otherwise, we accept the Null hypothesis. Thus, the value of  $\alpha$  affects how sure we are about the Null hypothesis. A smaller  $\alpha$  corresponds to more certain that Null hypothesis is wrong when it is rejected (the probability that Null hypothesis is true but it is rejected is  $\alpha$ , which is called type I error).

Since  $\chi = H_{\chi^2(n-r-1)}^{-1}(1 - \alpha)$  is a bijective, increasing function of  $1 - \alpha$  (nature of CDF), the greater value of  $\chi$ , the smaller value of  $\alpha$ . Furthermore, the Null hypothesis is rejected when  $g > \chi$ , the greatest value of  $\chi$  for which the Null hypothesis is accepted is  $\chi = g$ . This allows us to create a procedure for finding CPD that noise follows best as follows

1. Find  $g$  value of each distribution from (3.5).
2. Set  $\chi = g$ .
3. Find level of significance  $\alpha = 1 - H_{\chi^2(n-r-1)}(\chi)$ .
4. The CPD with the greatest  $\alpha$  is the one noise follows best.

For example, the Normal distribution has the greatest  $\alpha$  in the four distributions. When setting the level of significance equals value  $\alpha$  of Normal distribution, we can find the corresponding  $\chi$  of that alpha for all four distributions.  $g$  value of all four distributions

except Normal will be greater than the found values  $\chi$ . Thus, only Normal distribution assumption is not rejected and it can be seen as the distribution that noise follows best. The Matlab "chi2gof" function returns  $\alpha$  under variable named "p-value", which could be used to compare. In some cases, the return p-value is smaller than the smallest number that computers can represent. In such cases, the g values under a constraint can be used as an alternating method to find the best CPD. Assuming that the first distribution has greater degree than the second distribution, with the same value of  $\alpha$ ,  $\chi$  value of the first distribution will be greater than the one of the second distribution. The constraint is created such that if the degree of the first distribution is greater than or equal to the degree of the second distribution and g value of the first is smaller than that of the second distribution, the  $\alpha$  value of the first distribution will be greater than that of the second distribution, i.e. the first distribution is chosen.

The Kolmogorov-Smirnov test is another statistical test that computes the maximum discrepancy between empirical CDF and analytic CDF [22]. Matlab "kstest" function also returns p-value. As similar to the p-value of "chi2gof", the CPD with greatest p-value in kstest will be chosen. The best probability distributions fitted to all three axes and their corresponding  $\alpha$  (where possible), g values are shown in Table 3.3.

According to the  $\chi^2$ -test, t Location-Scale is the best distribution that models noise on x-axis (5 times best, 1 time second), Normal is the best distribution that noise on y-axis (2 times best, 3 times second) follows while Generalized Extreme Value is most suitable for z-axis (3 times best). Kolmogorov-Smirnov test yields a different conclusion, Normal is the best for both x (5 times best, 1 time second) and y (3 times best, 1 time second) axes while best distribution for z-axis is the same as  $\chi^2$ -test result. There occur the disagreement between the two statistical tests, this is due to the difference in the statistical properties of two tests (one deals with the maximal discrepancy in CDF while the other handles the total difference in PDF). The next section introduces the usage of statistical tests' results in calibration procedure.

### 3.4 Magnetometer Calibration method

The results of the previous section allow us to introduce noise vector by  $\epsilon_i = [\epsilon_{x,i} \ \epsilon_{y,i} \ \epsilon_{z,i}]^T$  (3.1) where the terms are

- $\epsilon_{x,i} \sim t(\mu_x, \sigma_x, \nu_x)$ ,  $\epsilon_{y,i} \sim \mathcal{N}(\mu_y, \sigma_y)$  and  $\epsilon_{z,i} \sim GEV(\mu_z, \sigma_z)$  using results of the  $\chi^2$ -test.
- $\epsilon_{x,i} \sim \mathcal{N}(\mu_x, \sigma_x)$ ,  $\epsilon_{y,i} \sim \mathcal{N}(\mu_y, \sigma_y)$  and  $\epsilon_{z,i} \sim GEV(\mu_z, \sigma_z)$  using results of the Kolmogorov-Smirnov tests.

where  $t$ ,  $GEV$ ,  $\mathcal{N}$  are t Location-Scale, Generalized Extreme Value and Normal distribution respectively.  $\mu_k$ ,  $\sigma_k$ ,  $\nu_k$  are location, scale and shape parameters on k-axis.

It is known that the correlation in noise between two axes requires further study and there exist a disagreement between the two statistical tests. Thus, to simplify the derived math-

**Table 3.3.** Best and second best probability distribution that noise follows on each axis, orientation from 2 statistical tests

Axis Orientation	$\chi^2$ test			Kolmogorov test		
	X	Y	Z	X	Y	Z
1	3379 (15)	$4.93 \cdot 10^{-65}$	1992 (17)	$3.24 \cdot 10^{-196}$	<u><math>8.66 \cdot 10^{-133}</math></u>	$6.87 \cdot 10^{-92}$
	<b>2227 (21)</b>	$2.98 \cdot 10^{-59}$	2020 (25)	$1.57 \cdot 10^{-130}$	$1.59 \cdot 10^{-161}$	$4.90 \cdot 10^{-97}$
	2482 (17)	<u><math>6.24 \cdot 10^{-09}</math></u>	<u>1735 (20)</u>	<u><math>7.94 \cdot 10^{-113}</math></u>	<b><math>1.10 \cdot 10^{-129}</math></b>	<b><math>2.58 \cdot 10^{-76}</math></b>
	<u>2274 (19)</u>	<b><math>1.87 \cdot 10^{-07}</math></b>	<b>1723 (21)</b>	<b><math>1.10 \cdot 10^{-106}</math></b>	$2.39 \cdot 10^{-133}$	<u><math>7.39 \cdot 10^{-84}</math></u>
2	3291 (17)	2681 (15)	<b>2860 (26)</b>	$4.49 \cdot 10^{-137}$	$1.15 \cdot 10^{-143}$	<b><math>7.26 \cdot 10^{-61}</math></b>
	<u>2589 (25)</u>	2885 (19)	3524 (35)	$1.89 \cdot 10^{-134}$	$5.61 \cdot 10^{-139}$	<u><math>9.06 \cdot 10^{-102}</math></u>
	2591 (20)	<b>2543 (17)</b>	3338 (30)	<b><math>1.90 \cdot 10^{-117}</math></b>	<b><math>2.39 \cdot 10^{-120}</math></b>	$7.42 \cdot 10^{-107}$
	<b>2448 (21)</b>	<u>2543 (16)</u>	3336 (30)	<u><math>2.14 \cdot 10^{-119}</math></u>	<u><math>2.39 \cdot 10^{-120}</math></u>	$4.53 \cdot 10^{-106}$
3	3533 (20)	2607 (14)	2753 (23)	$7.54 \cdot 10^{-156}$	$4.31 \cdot 10^{-142}$	$1.70 \cdot 10^{-74}$
	2812 (28)	2793 (19)	3034 (30)	$1.15 \cdot 10^{-125}$	$3.89 \cdot 10^{-177}$	<b><math>1.22 \cdot 10^{-66}</math></b>
	<u>2769 (21)</u>	<b>2479 (17)</b>	<b>2720 (26)</b>	<b><math>5.74 \cdot 10^{-94}</math></b>	<b><math>1.44 \cdot 10^{-140}</math></b>	$1.99 \cdot 10^{-74}$
	<b>2674 (23)</b>	<u>2479 (16)</u>	<u>2723 (25)</u>	<u><math>5.13 \cdot 10^{-108}</math></u>	<u><math>1.40 \cdot 10^{-140}</math></u>	<u><math>4.03 \cdot 10^{-73}</math></u>
4	6601 (23)	<b>5288 (35)</b>	<b>5578 (57)</b>	$2.32 \cdot 10^{-99}$	<b><math>7.28 \cdot 10^{-105}</math></b>	<b><math>9.67 \cdot 10^{-51}</math></b>
	6171 (30)	7130 (37)	7750 (58)	$2.70 \cdot 10^{-119}$	<u><math>1.82 \cdot 10^{-132}</math></u>	<u><math>1.36 \cdot 10^{-58}</math></u>
	<u>5887 (24)</u>	<u>6248 (37)</u>	6904 (58)	<b><math>7.59 \cdot 10^{-85}</math></b>	$2.21 \cdot 10^{-150}$	$2.27 \cdot 10^{-80}$
	<b>5866 (25)</b>	<u>6249 (36)</u>	6904 (57)	<u><math>1.56 \cdot 10^{-90}</math></u>	$2.04 \cdot 10^{-150}$	$2.34 \cdot 10^{-80}$
5	2789 (13)	2639 (14)	$2.60 \cdot 10^{-41}$	$8.78 \cdot 10^{-184}$	$9.98 \cdot 10^{-157}$	$4.69 \cdot 10^{-116}$
	2772 (17)	2675 (18)	$5.43 \cdot 10^{-80}$	$6.50 \cdot 10^{-180}$	$1.66 \cdot 10^{-154}$	$4.82 \cdot 10^{-109}$
	<u>2500 (16)</u>	<u>2491 (17)</u>	<b><math>2.71 \cdot 10^{-04}</math></b>	<b><math>2.86 \cdot 10^{-168}</math></b>	<u><math>4.80 \cdot 10^{-151}</math></u>	<b><math>1.58 \cdot 10^{-98}</math></b>
	<b>2493 (15)</b>	<b>2481 (16)</b>	<u><math>1.75 \cdot 10^{-04}</math></u>	<u><math>3.19 \cdot 10^{-169}</math></u>	<b><math>3.11 \cdot 10^{-149}</math></b>	<u><math>1.57 \cdot 10^{-98}</math></u>
6	$1.28 \cdot 10^{-137}$	2869 (12)	<b>2806 (22)</b>	$3.44 \cdot 10^{-186}$	<b><math>5.27 \cdot 10^{-140}</math></b>	<b><math>9.54 \cdot 10^{-63}</math></b>
	$1.23 \cdot 10^{-46}$	3137 (16)	3870 (26)	$1.15 \cdot 10^{-159}$	<u><math>2.95 \cdot 10^{-188}</math></u>	$6.72 \cdot 10^{-92}$
	<u>0.014</u>	2773 (14)	3060 (25)	<b><math>5.50 \cdot 10^{-134}</math></b>	$4.02 \cdot 10^{-201}$	$1.23 \cdot 10^{-87}$
	<b>0.041</b>	2773 (13)	3060 (24)	<u><math>1.64 \cdot 10^{-138}</math></u>	$4.43 \cdot 10^{-201}$	<u><math>1.56 \cdot 10^{-87}</math></u>

Four rows in each cell are (top to bottom): Generalized Extreme Value, Logistic, Normal and t Location-Scale.

**bold** and underline number represent the best and second best CPD respectively.

The number with another number in bracket shows g value and the degree of freedoms in  $\chi^2$ -test of the corresponding distribution. The other type of number is  $\alpha$  ( $\chi^2$  test) or p-value (Kolmogorov test)

Some cells contains no **bold** or/and underline since it is not possible to choose the better distributions (g values are approximately similar) and we cannot apply the constraint.

emational steps and just to show how the calibration works, we assume that noise on each axis is Gaussian with zero mean, identical standard deviation and independent to each other. By doing that, we can show that the calibration procedure partially denoise the measurements. Moreover, it can optimize the computational cost significantly by reducing the degree of freedom, which is also shown in this section. From this assumption, we have

$$\epsilon_i \sim \mathcal{N}(\mathbf{0}, \sigma^2 \mathbf{I}_{3 \times 3}) \xrightarrow{(3.3)} \mathbf{h}_{r,i} \sim \mathcal{N}(\mathbf{U}\Sigma\mathbf{h}_i^C + \mathbf{b}, \sigma^2 \mathbf{I}_{3 \times 3}) \quad (3.6)$$

The MLE is used to maximize the conditional probability of observed values given parameters  $(\mathbf{U}, \Sigma, \mathbf{b}) \in O(3) \times D^+(3) \times \mathbb{R}^3 := \Theta$  and  $\mathbf{h}_i^C \in S(3), i = 1, \dots, n$

$$\begin{aligned} & \max_{\substack{(\mathbf{U}, \Sigma, \mathbf{b}) \in \Theta \\ \mathbf{h}_i^C \in S(3), i=1, \dots, n}} p \{ \mathbf{h}_{r,i} | \mathbf{U}, \Sigma, \mathbf{h}_i^C, \mathbf{b} \} \\ & \stackrel{\text{i.i.d}}{=} \max_{\substack{(\mathbf{U}, \Sigma, \mathbf{b}) \in \Theta \\ \mathbf{h}_i^C \in S(3)}} \prod_{i=1}^n p \{ \mathbf{h}_{r,i} | \mathbf{U}, \Sigma, \mathbf{h}_i^C, \mathbf{b} \} \\ & = \max_{\substack{(\mathbf{U}, \Sigma, \mathbf{b}) \in \Theta \\ \mathbf{h}_i^C \in S(3)}} \prod_{i=1}^n \frac{e^{-\frac{1}{2}(\mathbf{h}_{r,i} - \mathbf{U}\Sigma\mathbf{h}_i^C - \mathbf{b})^T (\sigma^2 \mathbf{I})^{-1} (\mathbf{h}_{r,i} - \mathbf{U}\Sigma\mathbf{h}_i^C - \mathbf{b})}}{(2\pi|\sigma^2 \mathbf{I}|)^{1/2}} \\ & = \min_{\substack{(\mathbf{U}, \Sigma, \mathbf{b}) \in \Theta \\ \mathbf{h}_i^C \in S(3)}} \sum_{i=1}^n \|\mathbf{h}_{r,i} - \mathbf{U}\Sigma\mathbf{h}_i^C - \mathbf{b}\|^2 \\ & = \min_{\substack{(\mathbf{U}, \Sigma, \mathbf{b}) \in \Theta \\ \mathbf{h}_i^C \in S(3)}} \sum_{i=1}^n \left\| \mathbf{U}\Sigma \left( \Sigma^{-1} \mathbf{U}^T (\mathbf{h}_{r,i} - \mathbf{b}) - \mathbf{h}_i^C \right) \right\|^2 \\ & = \min_{\substack{(\mathbf{U}, \Sigma, \mathbf{b}) \in \Theta \\ \mathbf{h}_i^C \in S(3)}} \sum_{i=1}^n \left[ \mathbf{U}\Sigma \left( \Sigma^{-1} \mathbf{U}^T (\mathbf{h}_{r,i} - \mathbf{b}) - \mathbf{h}_i^C \right) \right]^T \left[ \mathbf{U}\Sigma \left( \Sigma^{-1} \mathbf{U}^T (\mathbf{h}_{r,i} - \mathbf{b}) - \mathbf{h}_i^C \right) \right] \\ & = \min_{\substack{(\mathbf{U}, \Sigma, \mathbf{b}) \in \Theta \\ \mathbf{h}_i^C \in S(3)}} \sum_{i=1}^n \left[ \left( \Sigma^{-1} \mathbf{U}^T (\mathbf{h}_{r,i} - \mathbf{b}) - \mathbf{h}_i^C \right) \right]^T (\mathbf{U}\Sigma)^T \mathbf{U}\Sigma \left[ \left( \Sigma^{-1} \mathbf{U}^T (\mathbf{h}_{r,i} - \mathbf{b}) - \mathbf{h}_i^C \right) \right] \\ & = \min_{\substack{(\mathbf{U}, \Sigma, \mathbf{b}) \in \Theta \\ \mathbf{h}_i^C \in S(3)}} \sum_{i=1}^n \left[ \left( \Sigma^{-1} \mathbf{U}^T (\mathbf{h}_{r,i} - \mathbf{b}) - \mathbf{h}_i^C \right) \right]^T \left[ \left( \Sigma^{-1} \mathbf{U}^T (\mathbf{h}_{r,i} - \mathbf{b}) - \mathbf{h}_i^C \right) \right] \\ & = \min_{\substack{(\mathbf{U}, \Sigma, \mathbf{b}) \in \Theta \\ \mathbf{h}_i^C \in S(3)}} \sum_{i=1}^n \left\| \Sigma^{-1} \mathbf{U}^T (\mathbf{h}_{r,i} - \mathbf{b}) - \mathbf{h}_i^C \right\|^2 \end{aligned} \quad (3.7)$$

Minimum of (3.7) is computed iteratively using Newton-like or gradient methods. However, the search space is large since we need to estimate  $n$  magnetic field vectors  $\mathbf{h}_i^C$ . The search space is then  $2n + \dim(\Theta) = 2n + \dim(O(3)) + \dim(D^+(3)) + \dim(\mathbb{R}^3) = 2n + 9$ , which has already taken into account the constraint that norm of magnetic field vectors  $\mathbf{h}_i^C$  are 1. Thus, dimension of each magnetic field vector is  $\dim(\mathbf{h}_i^C) = 3 - (1 \text{ constraint}) = 2$ . The minimization problem (3.7) can be rewritten to search only in the parameter space  $\Theta$  since the solution  $(\mathbf{U}^*, \mathbf{\Sigma}^*, \mathbf{b}^*)$  also minimizes

$$\min_{(\mathbf{U}, \mathbf{\Sigma}, \mathbf{b}) \in \Theta} \sum_{i=1}^n \left( \left| \left| \mathbf{\Sigma}^{-1} \mathbf{U}^T (\mathbf{h}_{r,i} - \mathbf{b}) \right| \right| - 1 \right)^2 \quad (3.8)$$

Proof of (3.8) can be found in [33]. Finally, minimization problem (3.8) can be formulated on the Euclidean space, which allows for the use of optimization tools for unconstrained problems [10].

$$\min_{\mathbf{A} \in \mathbb{R}^{3 \times 3}, \mathbf{b} \in \mathbb{R}^3} \sum_{i=1}^n \left( \left| \left| \mathbf{A} (\mathbf{h}_{r,i} - \mathbf{b}) \right| \right| - 1 \right)^2 \quad (3.9)$$

with the solution  $\mathbf{A}^*, \mathbf{b}_A^*$ . When we take the SVD decomposition  $\mathbf{A}^* = \mathbf{U}_A^* \mathbf{\Sigma}_A^* \mathbf{V}_A^{*T}$ , the solution of (3.8) is given by  $\mathbf{U}^* = \mathbf{V}_A^*, \mathbf{\Sigma}^* = \mathbf{\Sigma}_A^{*-1}, \mathbf{b}^* = \mathbf{b}_A^*$ . The unconstrained optimization problem (3.9) can be solved using Newton-like or gradient method in Euclidean space [6].

The initial guess is the vital factor in reducing the time of finding the optimal solution. Several fitting techniques have been proposed in order to find the solution faster. Most of them are derived under Least Squares (LS) Framework that try to create a pseudo-least square problem which is called algebraic fitting method [8], [11]. It is implemented by A. Barraud and S. Leseq in Matlab[14]. The algorithm yields two coefficients  $\mathbf{X}, \mathbf{y}$  that could be used directly as initial guess  $\mathbf{A}_0 = \mathbf{X}, \mathbf{b}_0 = \mathbf{y}$  in optimization problem (3.9).

Given the optimal solution of (3.9) as  $\mathbf{U}^*, \mathbf{\Sigma}^*, \mathbf{b}^*$ , the unbiased and unit norm vector representing the Earth magnetic field in calibration frame  $\{C\}$  is obtained by manipulating equation (3.3)

$$\mathbf{h}_i^C = \mathbf{\Sigma}^{-1} \mathbf{U}^T (\mathbf{h}_{r,i} - \mathbf{b}) \quad (3.10)$$

### 3.5 Alignment algorithm

In order to find the geomagnetic field in the sensor frame  $\{S\}$ , one needs the orthogonal matrix  $\mathbf{V}$  mentioned in Section 3.2. This alignment is independent from the calibration procedure. It requires external heading sources or localization systems. In [33], the step by step procedure to obtain  $\mathbf{V}$  in the Least Square framework is discussed. The estimated  $\hat{\mathbf{V}}$  helps transforming measurements from the calibration frame  $\{C\}$  to an Optimized-Sensor  $\{OS\}$  frame.

Next section represents the results and analysis of simulation and experimental setup that apply the calibration procedure.

## 4 RESULT AND ANALYSIS

### 4.1 Simulation results

The simulated data is first used to analyze the efficiency of calibration algorithm. The randomly picked values of parameters of error sources described in Section 3.1 are

$$\mathbf{T}_{SF} = \text{diag} \left( \begin{bmatrix} 1.0 \\ 1.5 \\ 1.2 \end{bmatrix} \right), \mathbf{T}_{NO} = \begin{bmatrix} 1.000 & 0.000 & 0.000 \\ 0.174 & 0.985 & 0.000 \\ -0.174 & 0.086 & 0.981 \end{bmatrix}, \mathbf{T}_{SI} = \begin{bmatrix} 0.58 & -0.73 & 0.36 \\ 1.32 & 0.46 & -0.12 \\ -0.26 & 0.44 & 0.53 \end{bmatrix}$$

$$\mathbf{b}_{HI} = \begin{bmatrix} -1.5 \\ 4.0 \\ 2.0 \end{bmatrix} G, \mathbf{b}_{SO} = \begin{bmatrix} 1.5 \\ 0.4 \\ 6.0 \end{bmatrix} G, \mathbf{h}_{LLF} = \begin{bmatrix} 0.0 \\ 0.0 \\ 0.6 \end{bmatrix} G, \sigma = 10mG$$

The artificial magnetometer is supposed to rotate  $360^\circ$  around the z-axis in LLF, i.e. sweep yaw angle  $\in [0, 360]^\circ$ , and  $180^\circ$  around the x-axis (sweep pitch angle). In total  $10^4$  simulated measurements are produced with additive zero mean,  $10mG$   $\sigma$  standard deviation - Gaussian random noise. The simulated data for error-free magnetometer and artificial magnetometer are shown in Figure 4.1.

The likelihood function  $f$  is normalized by the number of samples  $n$ . The Matlab built-in function "fminunc" is used for this unconstrained optimization problem. Default values are used for the step size and the terminal condition. Quasi-Newton iterative algorithm is used. As mentioned in section 3.5, the calibrated magnetic measurements are in the  $\{C\}$  frame, it is not aligned with true magnetic field in the sensor frame. Knowing the true magnetic measurements in the sensor frame from simulated data, one could apply the alignment procedure in section 3.5 to observe the calibrated measurements in the  $\{OS\}$  frame (Fig. 4.2).

Initially, likelihood function  $f$  is very large for non-calibrated data  $f(x_e)$ . Using initial guess parameters  $\mathbf{A}_0$  and  $\mathbf{b}_0$  already improves likelihood function more than  $10^6$  times. After the calibration procedure, likelihood function is further reduced by 14% with only 29 iterations. Let us define the Euclidean distance between the estimated and true parameters, this means  $b_{LS} = \|\mathbf{b}_0 - \mathbf{b}_{true}\|_2$  and  $b_{MLE} = \|\mathbf{b}^* - \mathbf{b}_{true}\|_2$ . Table 4.1 shows that the MLE method in Calibration procedure also improves the accuracy compared to initial guess

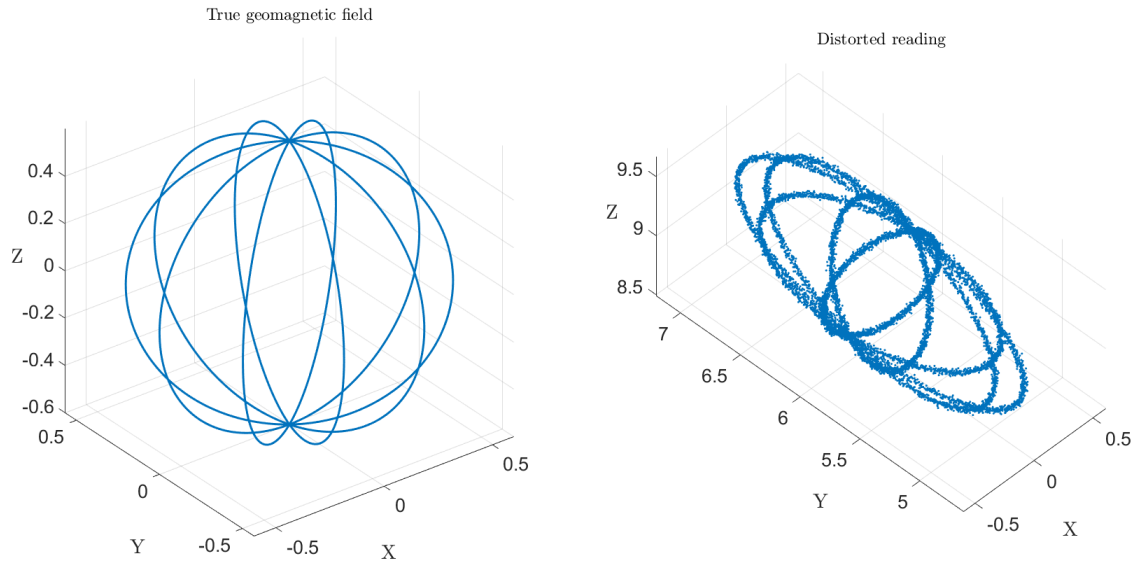


**Figure 4.1.** Simulation data of True and distorted magnetic field

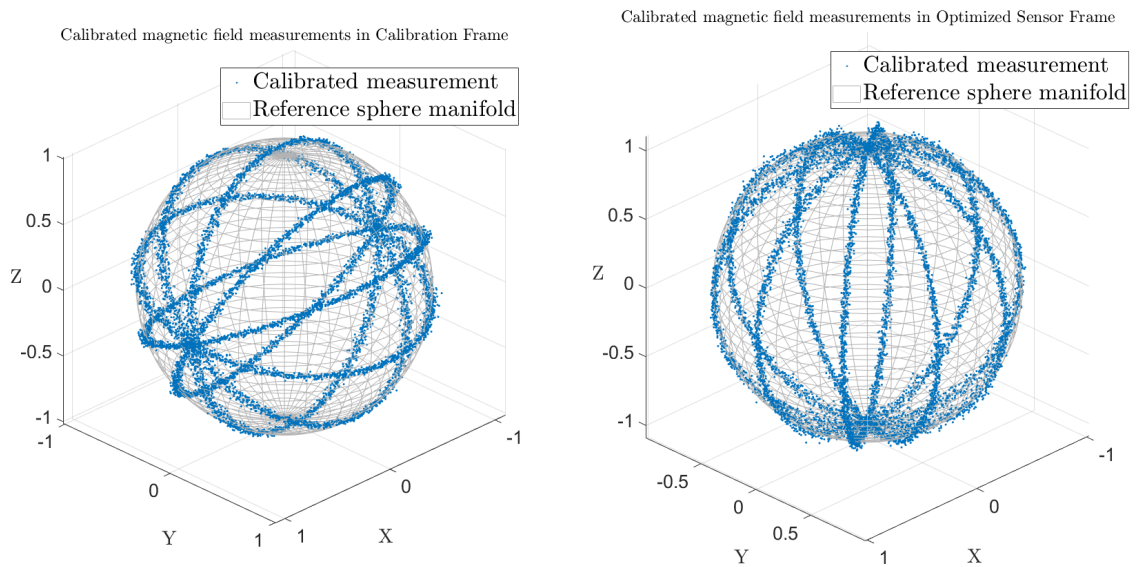


**Figure 4.2.** Simulation data of Calibrated magnetic field in Calibration and Optimized Sensor Frame

using the Least Square method.

In real-world situations, the sole calibration algorithm should help determine the heading angle of the magnetometer without being aligned every time by using an external source. Although the alignment procedure only uses the first 2000 noiseless simulated geomagnetic measurements in the sensor frame, it can already estimate the orthogonal matrix  $V$

**Table 4.1.** Calibration results

$f(x_e)$	$f(x_0)$	$f(x^*)$	iterations	$b_{LS}$	$b_{MLE}$
97.3626	$4.0326 \times 10^{-4}$	$4.0066 \times 10^{-4}$	29	$4.7941 \times 10^{-4}$	$4.1307 \times 10^{-4}$

accurately enough to transform the remaining 8000 noisy calibrated measurements from  $\{C\}$  frame to  $\{OS\}$  frame. Figure 4.3 shows the differences of true geomagnetic field and aligned-calibrated magnetic field provided that the first 2000 true field values are known. The mean value of difference is  $0.01 \mu T$ , which is significantly smaller than the resolution of the real magnetometer used in this work. Note that we also need to know the norm of the geomagnetic field at that point (in this simulation, it is  $0.6 \mu T$ ) since the calibration procedure maps measurements to unit sphere.

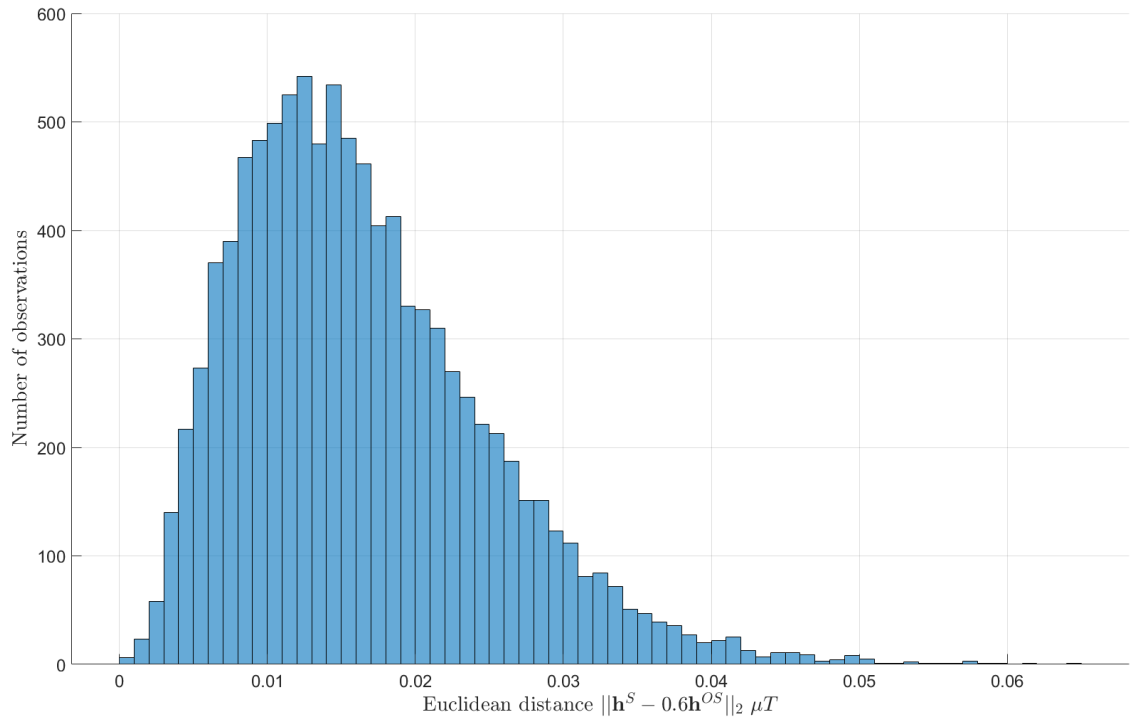


**Figure 4.3.** Histogram of Euclidean distance between aligned-calibrated and true magnetic field

## 4.2 Experimental results

The experimental device is the same as the one used in Section 3.3.2. The acquisition unit and its properties remain.

The device is rotated in a random manner in one location to cover the full ellipsoidal manifold. The norm of reference geomagnetic spherical manifold on measurement day is extracted from the WMM geomagnetic model [20] with the given coordinates. Figure 4.4 shows the magnetic field measurements and the reference geomagnetic-norm sphere.

From this figure, the most trivial error effect is the combination of sensor sensitivity and soft iron since the raw measurements fall out of the reference sphere. Only four iterations are needed to find the calibration parameters, the found bias term is  $\mathbf{b}^* = [-0.06, -0.17, 0.06]^T \mu T$ . The bias term is small since there are no external magnetic sources nearby. The error matrices such as Non-orthogonal, Scale factor, etc, cannot be separated from the estimated matrices. Hence, it is not worth showing values of  $\Sigma$  and

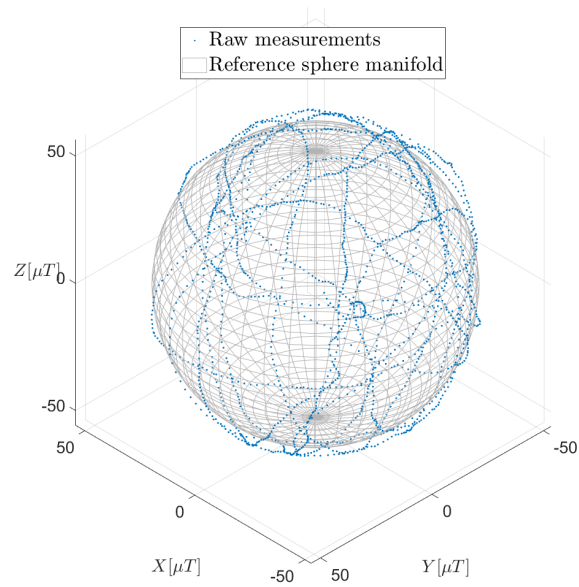


**Figure 4.4.** Raw data with the sphere manifold reference

$\mathbf{U}$  since they provide no information for the error source. The norm of calibrated magnetometer data is compared with the norm of normalized raw data as shown in Figure 4.5. With a standard deviation of 0.011 for calibrated norm and 0.016 for normalized raw data, the calibration algorithm has reduced the variation by more than 30%. It thus enables denoising and partially compensates errors.

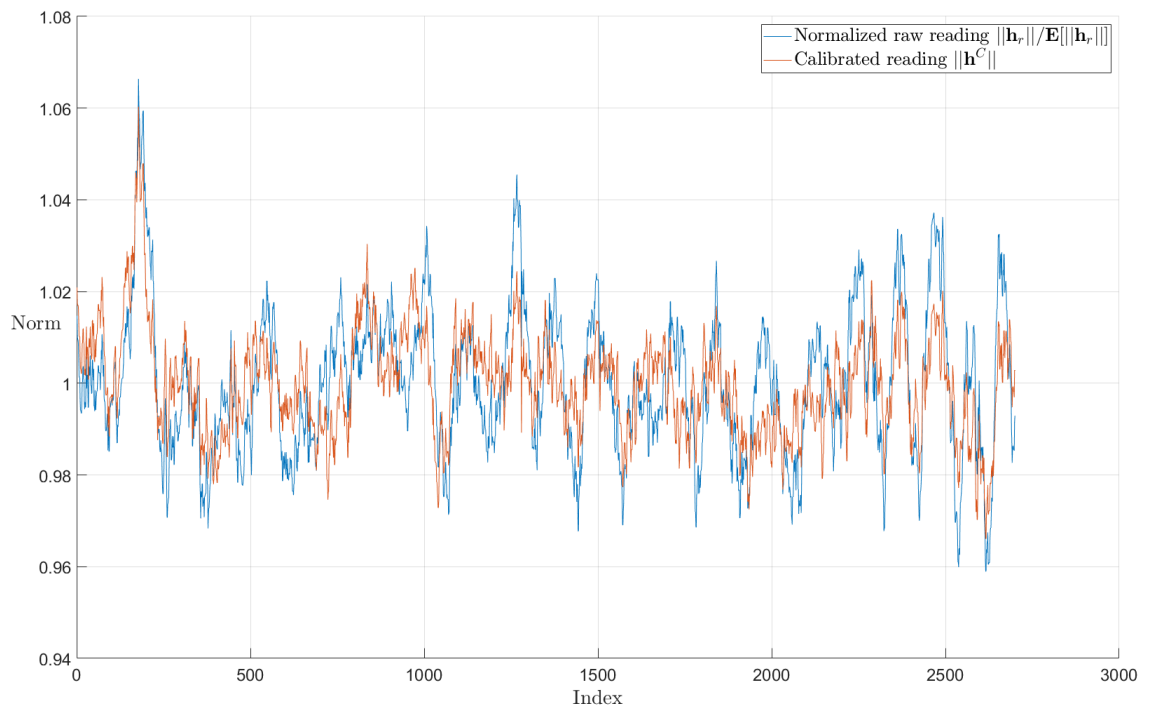


**Figure 4.5.** Norm of calibrated data compared to raw data

## 5 CONCLUSION AND FUTURE WORK

Using probability distributions to model noise in sensors provides the mean to understand noise under a mathematical formulation. This technique also allows utilizing the MLE framework in estimating error parameters. Otherwise, sensor noise is still an obscure phenomena that could not be tackled.

The proposed algorithm to find optimal bin width which assumes no reason in the flawless of measurements still ensures that statistical tests are applicable. Although state-of-the-art research assumes the Normal distribution with same standard deviation for readings on all three axes, statistical tests in this thesis disprove this assumption. Further developments of the likelihood function are needed. At least, Normal distributions with different standard deviations for each axis should be studied. Due to the abnormality in sensor reading being application-dependent, further studies analyzing this irregularity is required, and a more suitable algorithm should be derived.

Solving the unconstrained optimization problem by "fminunc" function also showed that the estimated result is wrong without the good initial guess. This is due to the nature of the likelihood function. Because it is non-convex the function might get stuck at a local minimum. Although the initial guess is available from existing work, it is worth mentioning the diversity in initial guess parameters because of the quadratic form in , e.g. Equation 3.9

$$\sum_{i=1}^n \left( \left\| \mathbf{A}(\mathbf{h}_{r,i} - \mathbf{b}) \right\| - 1 \right)^2 = \sum_{i=1}^n \left( \left\| \mathbf{h}_i^C + \mathbf{A}\epsilon_i \right\| - 1 \right)^2 = \sum_{i=1}^n \left( \dots + \epsilon_i^T \mathbf{A}^T \mathbf{A} \epsilon_i \right)$$

The expectation of the quadratic in noise term is  $\mathbb{E}(\epsilon_i^T \mathbf{A}^T \mathbf{A} \epsilon_i) \geq 0$ . That make the least square approach statistically inconsistent. In [25], this inconsistency has been mentioned and the Adaptive Least Squares (ALS) algorithm has been proposed to overcome the problem. As an introduction to magnetometer calibration, this thesis does not use the ALS algorithm but an already implemented algorithm. However, the author recommends others to implement the ALS.

The calibration algorithm reduced the uncertainty in magnetic measurements in the experiment. In order to obtain lower standard deviation, better probability distributions should be chosen for noise on each axis. Because the best CPDs proposed by the  $\chi^2$ -test are different from those proposed by the Kolmogorov-Smirnov test, no final decision on which distributions to use was made. The Akaike information criterion that was founded on information theory will be, in that case, a better standard to evaluate the best fitted distributions. After choosing the best fitted distribution for each axis, the new likelihood

function could be derived. Then, further mathematical manipulations could be developed for this specific case to simplify the optimization function.

Simulation data demonstrated the effects of each error type by matrices and the calibration algorithm compensated the influence of those effects. Using a part of true readings as reference heading sources shows the applicable scenario: The magnetometer that we are interested in only needs heading reference unit in a short time, then it can self calibrate and align. The experimental data, likewise, shows the effect of calibration method. The interference of error sources are not trivial since the readings almost fall on the sphere. This is because the used magnetometer is released recently in the market (2017) and still integrated in new smartphone of 2019. While a lot of older devices use less modern magnetometer, which causes more significant errors. Simulation and experiment are done with measurements that diverse in three dimension to guarantee there exist a unique fitted ellipsoid. If measurements only cover a circle, there are infinite ellipsoids that these measurements lie on. The figure-8 pattern is, though simple, sufficient for the calibration algorithm to find unique parameters of ellipsoid. As shown in Figure 5.1, figure-8 pattern measurements already cover the sphere.

Besides the aforementioned tasks, future work includes using high-grade magnetome-

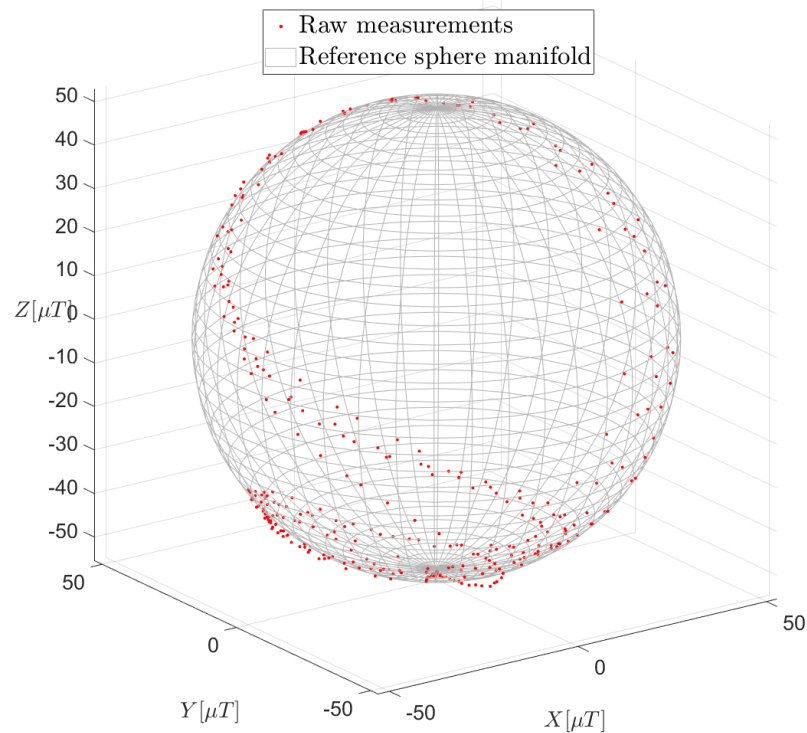


**Figure 5.1.** raw data of Figure-8 pattern in 3D space

ters to evaluate the performance of calibrated algorithm experimentally. These magnetometers can also be used as a reference unit in the alignment procedure.

## REFERENCES

- [1] *A Dictionary of Physics (6th Edition)*. Dictionary. Oxford University Press, 2012. URL: <https://en.oxforddictionaries.com/definition/us/>.
- [2] N. G.-I. Agency. *The American Practical Navigator: Bowditch*. Skyhorse Publishing Company, Incorporated, 2013. ISBN: 9781620877968. URL: <https://books.google.fi/books?id=rSBdNAEACAAJ>.
- [3] *Android device sensor frame*. May 20, 2019. URL: [https://developer.android.com/guide/topics/sensors/sensors\\_overview](https://developer.android.com/guide/topics/sensors/sensors_overview) (visited on 05/31/2019).
- [4] *AndroSensor application*. May 1, 2019. URL: <https://play.google.com/store/apps/details?id=com.fivasim.androsensor&hl=en> (visited on 05/31/2019).
- [5] N. Balakrishnan and D. Kundu. Birnbaum-Saunders Distribution: A Review of Models, Analysis and Applications. In: *arXiv e-prints*, arXiv:1805.06730 (May 2018), arXiv:1805.06730. arXiv: 1805.06730 [stat.ME].
- [6] S. Boyd and L. Vandenberghe. *Convex optimization*. Cambridge university press, 2004.
- [7] *Earth magnetic field and Earth's geography*. May 20, 2019. URL: <https://www.met.ie/science/valentia/geomagnetism> (visited on 06/11/2019).
- [8] J. Fang, H. Sun, J. Cao, X. Zhang, and Y. Tao. A novel calibration method of magnetic compass based on ellipsoid fitting. In: *IEEE Transactions on Instrumentation and Measurement* 60.6 (2011), 2053–2061.
- [9] *Figure 8 pattern in phone*. May 20, 2019. URL: <https://forums.androidcentral.com/samsung-galaxy-note-5/570264-compass-problem.html> (visited on 07/03/2019).
- [10] R. Fletcher. *Practical methods of optimization*. John Wiley & Sons, 2013.
- [11] C. C. Foster and G. H. Elkaim. Extension of a two-step calibration methodology to include nonorthogonal sensor axes. In: *IEEE Transactions on Aerospace and Electronic Systems* 44.3 (2008), 1070–1078.
- [12] R. Hyndman. *The problem with Sturges' rule for constructing histograms*. Jan. 1995. URL: <https://robjhyndman.com/publications/sturges/>.
- [13] P. Lax. *Functional Analysis*. Pure and Applied Mathematics: A Wiley Series of Texts, Monographs and Tracts. Wiley, 2014. ISBN: 9781118626740. URL: [https://books.google.fi/books?id=e%5C\\_BjBAAAQBAJ](https://books.google.fi/books?id=e%5C_BjBAAAQBAJ).
- [14] *Least Square magnetic calibration toolbox*. May 20, 2019. URL: [https://se.mathworks.com/matlabcentral/fileexchange/23398-magnetometers-calibration?s\\_tid=prof\\_contriblnk](https://se.mathworks.com/matlabcentral/fileexchange/23398-magnetometers-calibration?s_tid=prof_contriblnk) (visited on 05/31/2019).
- [15] E. W. Lee. *Magnetism: an introductory survey*. Courier Corporation, 1970.
- [16] *Magnetometer Sensor*. May 20, 2019. URL: <https://www.digikey.com/catalog/en/partgroup/ak09918/70323> (visited on 05/31/2019).

- [17] P. P. de Maricourt. *The letter of Peter Peregrinus de Maricourt to Sygerus de Foucaucourt, soldier, concerning the magnet*. non-specific, 1943.
- [18] MATLAB. *version 9.6.0.1072779 (R2019a)*. The MathWorks Inc., 2019.
- [19] R. Merrill and M. W. McElhinny. The Earth's Magnetic Field. Its History, Origin and Planetary Perspective. In: *International Geophysics Series* 122 (Jan. 1983). DOI: 10.1017/S0016756800031630.
- [20] *NCEI Geomagnetic Calculators*. May 20, 2019. URL: <https://www.ngdc.noaa.gov/geomag/calculators/magcalc.shtml#igrfwmm> (visited on 05/31/2019).
- [21] A. Noureldin, T. B. Karamat, and J. Georgy. Basic Navigational Mathematics, Reference Frames and the Earth's Geometry. In: *Fundamentals of Inertial Navigation, Satellite-based Positioning and their Integration*. Berlin, Heidelberg: Springer Berlin Heidelberg, 2013, 21–63. ISBN: 978-3-642-30466-8. DOI: 10.1007/978-3-642-30466-8\_2. URL: [https://doi.org/10.1007/978-3-642-30466-8\\_2](https://doi.org/10.1007/978-3-642-30466-8_2).
- [22] J. Ogden, M. Fogiel, Research, E. Association, Research, E. A. (Piscataway)., and T. Rea. *The Statistics Problem Solver*. Problem Solvers Solution Guides. Research and Education Association, 1978. ISBN: 9780878915156. URL: <https://books.google.fi/books?id=ULJEbqznidoC>.
- [23] H. Q. P. Guo and Y. Yang. The soft iron and hard iron calibration method using extended Kalman filter for attitude and heading reference system. In: *IEEE Position Location Navig. Symp. 2008*, 1167–1174.
- [24] D. Poole. *Linear Algebra: A Modern Introduction*. Thomson; Brooks Cole, 2006.
- [25] V. Renaudin, M. H. Afzal, and G. Lachapelle. Complete triaxis magnetometer calibration in the magnetic domain. In: *Journal of sensors 2010* (2010).
- [26] D. W. Scott. Sturges' and Scott's Rules. In: *International Encyclopedia of Statistical Science*. Ed. by M. Lovric. Berlin, Heidelberg: Springer Berlin Heidelberg, 2011, 1563–1566. ISBN: 978-3-642-04898-2. DOI: 10.1007/978-3-642-04898-2\_578. URL: [https://doi.org/10.1007/978-3-642-04898-2\\_578](https://doi.org/10.1007/978-3-642-04898-2_578).
- [27] D. W. Scott. Multivariate density estimation and visualization. In: *Handbook of computational statistics*. Springer, 2012, 549–569.
- [28] *Sensor Record app*. May 20, 2019. URL: [https://play.google.com/store/apps/details?id=de.martingolpashin.sensor\\_record&hl=en](https://play.google.com/store/apps/details?id=de.martingolpashin.sensor_record&hl=en) (visited on 05/31/2019).
- [29] H. Shimazaki and S. Shinomoto. A method for selecting the bin size of a time histogram. In: *Neural computation* 19.6 (2007), 1503–1527.
- [30] D. Sobel. *Longitude: The true story of a lone genius who solved the greatest scientific problem of his time*. Macmillan, 2005.
- [31] J. Stepišnik. NMR down to Earth. In: *Nature, International journal of science* 800.439 (2006), 799.
- [32] J. Tomczyński, T. Mańkowski, and P. Kaczmarek. Cross-Sensor Calibration Procedure for Magnetometer and Inertial Units. In: *International Conference Automation*. Springer. 2017, 450–459.

- [33] J. Vasconcelos, G. Elkaim, C. Silvestre, P. Oliveira, and B. Cardeira. A geometric approach to strapdown magnetometer calibration in sensor frame. In: *IFAC Proceedings Volumes* 41.1 (2008), 172–177.
- [34] G. Vasilescu. *Electronic noise and interfering signals: principles and applications*. Springer Science & Business Media, 2006.
- [35] N. Weiss. Dynamism in planets, stars and galaxies. In: *Astronomy Geophysics* 43.3 (June 2002), 3.9–3.14. ISSN: 1366-8781. DOI: 10.1046/j.1468-4004.2002.43309.x. eprint: <http://oup.prod.sis.lan/astrogeo/article-pdf/43/3/3.9/478556/43-3-3.9.pdf>. URL: <https://doi.org/10.1046/j.1468-4004.2002.43309.x>.
- [36] H. D. Young. *university physics: with modern physics*. Pearson Addison Wesley, 2004.

## A FRAME OF REFERENCE

This appendix gives an overview of popular frames of reference and definition of each frame. For a more thorough discussion, readers can refer to [21].

A coordinate of a three-dimensional vector  $\mathbf{r}$  in arbitrary frame  $k$  is depicted as

$$\mathbf{r}^k = [x^k \ y^k \ z^k]^T$$

where  $x^k$ ,  $y^k$ ,  $z^k$  are the coordinates on x,y and z axis of vector  $\mathbf{r}$  respectively.

The three most used frames of reference are Earth-fixed Frame, Local Level Frame (LLF) and Body or Sensor Frame [21]. The Earth-fixed frame is defined by

- The origin is at the center of mass of the Earth.
- The z-axis passes through the conventional terrestrial pole.
- The x-axis passes through the intersection of the equatorial plane and the reference meridian (i.e. the Greenwich meridian).
- The y-axis completes the right-hand coordinate system in the equatorial plane.

This frame of reference is used for objects that stay stationary with respect to the rotation of the Earth. For instance, a geostationary satellite is a satellite in geosynchronous orbit, with an orbital period the same as the Earth's rotation period. This frame simplifies the calculation related to that satellite since coordinates of the satellite are constant in this frame.

The LLF is defined as follows

- The origin coincides with the center of the sensor frame (origin of inertial sensor triad).
- The y-axis points to true north.
- The x-axis points to east.
- The z-axis completes the right-handed coordinate systems by pointing up, perpendicular to the reference ellipsoid.

This frame of reference is used to represent a vehicle's attitude and velocity when it is on or near the surface of the Earth. The reference magnetic field from [20] uses this frame to provide the value of the magnetic field vector at a location on Earth. The relations between those frames are shown in Fig. A.1.

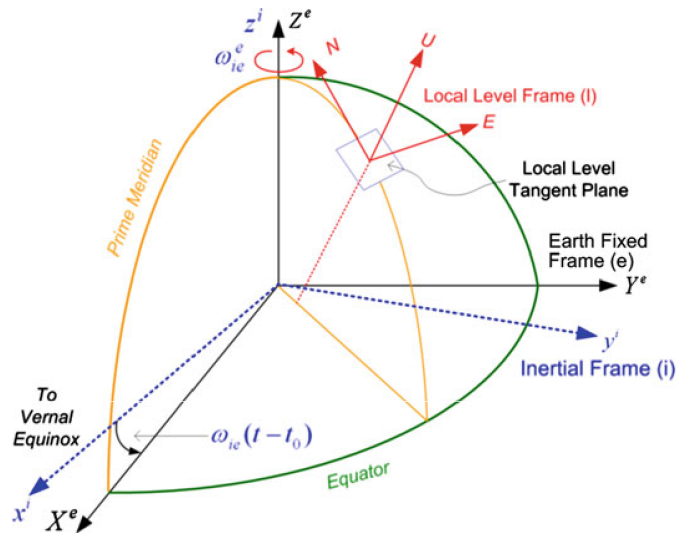


**Figure A.1.** The relationship between different common used reference frames

The third important frame of reference is sensor or body frame. The tri-axial magnetometer reading is from Android device. Android Sensor documentation defines the sensor frame as "When a device is held in its default orientation, the X axis is horizontal and points to the right, the Y axis is vertical and points up, and the Z axis points toward the outside of the screen face" [3] as shown in Figure (A.2).

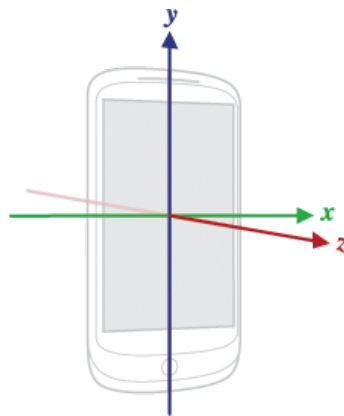


**Figure A.2.** Sensor frame of reference

More frames of reference and their usage can be found in [21].